AIAA JOURNAL
Vol. 46, No. 9, September 2008

Insect-Based Hover-Capable Flapping Wings for Micro Air Vehicles: Experiments and Analysis

Beerinder Singh* and Inderjit Chopra†
University of Maryland, College Park, Maryland 20742

DOI: 10.2514/1.28192

This paper addresses the aerodynamics of insect-based, biomimetic, flapping wings in hover. An experimental apparatus, with a biomimetic flapping mechanism, was used to measure the thrust generated by a number of wing designs at different wing pitch settings. To quantify the large inertial loads acting on the wings, vacuum chamber tests were conducted. Results were obtained for several high-frequency tests conducted on lightweight aluminum and composite wings. The wing mass was found to have a significant influence on the maximum frequency of the mechanism because of a high inertial power requirement. All the wings tested showed a decrease in thrust at high frequencies. In contrast, for a wing held at 90-deg pitch angle, flapping in a horizontal stroke plane with passive pitching caused by aerodynamic and inertial forces, the thrust was found to be larger. To study the effect of passive pitching, the biomimetic flapping mechanism was modified with a passive torsion spring on the flapping shaft. Results of some tests conducted with different wings and different torsion spring stiffnesses are shown. A soft torsion spring led to a greater range of pitch variation and produced more thrust at slightly lower power than with the stiff torsion spring. The lightweight and highly flexible wings used in this study had significant aeroelastic effects which need to be investigated. A finite element based structural analysis of the wing is described, along with an unsteady aerodynamic analysis based on indicial functions. The analysis was validated with experimental data available in literature, and also with experimental tests conducted on the biomimetic flapping–pitching mechanism. Results for both elastic and rigid wing analyses are compared with the thrust measured on the biomimetic flapping–pitching mechanism.

Nomenclature

A_n	=	aerodynamic coefficient
B_n^p	=	elastic aerodynamic influence coefficient for mode p
$\mathbf{C}$	=	damping matrix
c	=	chord
D	=	drag, per unit span
$\mathbf{F}$	=	force vector
F_i	=	inertial force, per unit span
F_n	=	force normal to wing chord, per unit span
F_x	=	force tangential to wing chord, per unit span
F^c	=	circulatory force
F^k	=	force caused by shed wake (Kussner effect)
F^{nc}	=	noncirculatory force
F^{pol}	=	Polhamus force
i, j, k	=	unit vectors
$\mathbf{K}$	=	stiffness matrix
L	=	lift, per unit span
$\mathbf{M}$	=	mass matrix
m	=	mass
N_m	=	total number of modes
p	=	mode number
$\mathbf{q}$	=	generalized coordinates
Re	=	Reynolds number, $V_{\text{tip}}c/\nu$
$\mathbf{r}$	=	position vector
r	=	spanwise coordinate
T	=	time period of one flap cycle
$\mathbf{T}_{(\cdot)}$	=	transformation matrix
t	=	time
U	=	strain energy
$\mathbf{V}$	=	velocity vector at a point on the wing
$V_{(\cdot)}$	=	flow velocity
v_i	=	induced inflow velocity
v_n	=	velocity normal to wing chord
v_x	=	velocity tangential to wing chord
w	=	out of plane deformation
x, y, z	=	coordinates in the pitching reference frame
α	=	angle of attack
β	=	wing flapping angle
Γ	=	circulation
γ	=	vorticity strength
Δt	=	duration of acceleration
ϵ	=	strain vector
θ	=	wing pitch angle
κ	=	vector of curvatures
ν	=	kinematic viscosity
ρ	=	mass density
ϕ_w	=	Wagner function
ψ_k	=	Kussner function

Received 4 October 2006; revision received 29 October 2007; accepted for publication 9 November 2007.

*Graduate Research Assistant, Alfred Gessow Rotorcraft Center; currently Scientist, Metacomp Technologies Inc.; bsingh@metacomptech.com.

†Alfred Gessow Professor and Director, Alfred Gessow Rotorcraft Center, Department of Aerospace Engineering.

Introduction

RECENT advances in microtechnologies, such as micro-electromechanical systems (MEMS), have led to the development of miniature charge-coupled device (CCD) cameras, tiny infrared sensors, and chip-sized hazardous substance detectors. These developments have led to significant interest in miniature flying vehicles called micro air vehicles (MAVs), which can act as highly portable platforms for these miniature sensors [1]. The low detectability and low noise promised by MAVs, their ability to transmit real-time data from an area of observation, and their ability to maneuver within confined spaces make them ideal for a variety of military and civilian missions. An MAV is defined by its maximum dimension of 15 cm and an all-up weight of 100 g, although this definition, set by the Defense Advanced Research Projects Agency (DARPA) in 1997, has become quite flexible in recent years.

In some ways, MAV development is analogous to the development of their manned counterparts over the last century, with fixed-wing vehicles further ahead in the developmental stages as compared to rotary or flapping wing vehicles. This is mainly

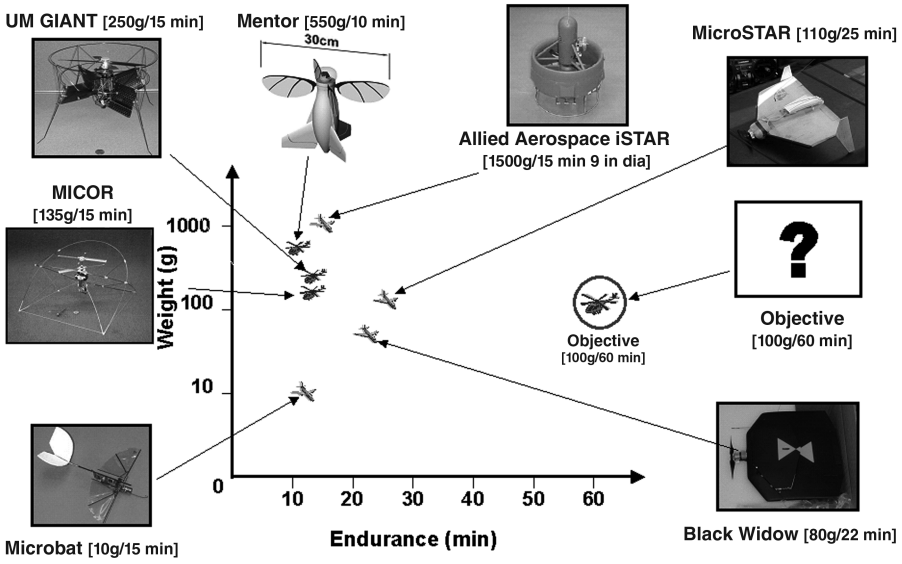

Fig. 1 Existing MAVs (2005 data).

because wing rotation introduces added complexity to the analysis, design, and fabrication of rotary wing vehicles. Flapping wings represent another jump in complexity because the wings are not only moving with respect to the vehicle but also accelerating and decelerating continuously, leading to a highly unsteady flow regime. Figure 1 shows the performance of some existing MAVs against the size and weight parameters set by DARPA. In terms of endurance, fixed-wing MAVs such as the Aerovironment Black Widow [2], outperform rotary and flapping wing MAVs. However, their major shortcoming is the lack of hover capability, which allows an MAV to maneuver in much smaller confined spaces, and more important, to perch and observe while saving valuable battery power. It is evident from Fig. 1 that all the hover-capable MAVs, such as Micor [3] and Mentor, have low endurance and high weight. Mentor and Microbat [4] are the two flapping wing MAVs shown in Fig. 1. Mentor uses a phenomenon called "clap fling," which is used by a few species of insects to hover. However, because of the clapping of its wings, it has an adverse noise signature. The Microbat is a 12-g vehicle, but it has low endurance and is also incapable of hovering flight.

In nature, flight has evolved into two different forms—insect flight and bird flight. Although both of these forms are based on flapping wings, there are important differences among them. Most birds flap their wings in a vertical plane without large changes (>90 deg) in the pitch of the wings during a flapping cycle. As a result, most birds cannot hover because they need a forward velocity to generate sufficient lift. The Caltech-Aerovironment Microbat is based on this type of birdlike flapping, thus, it cannot hover. However, the insect world abounds with examples of hovering flight. In hover, these insects flap their wings in a nearly horizontal plane (Fig. 2), accompanied by large changes in wing pitch angle to produce lift even in the absence of any forward velocity. Although insect wing beat kinematics vary widely between species, most two-winged, hover-capable insects exhibit some variation of this basic kinematic pattern. Among insects, there exist animals that are capable of taking off backward, flying sideward, and landing upside down. Moreover, birds such as the hummingbird, which are capable of hovering, have wing motions very similar to hover-capable insects. Thus, insect-based biomimetic flight may present a hover-capable and highly maneuverable solution for MAVs.

The distinction between birdlike flapping, henceforth referred to as ornithoptic flapping, and insect-based, or hover-capable flapping, is also important for another reason. Ornithoptic flapping requires a much simpler mechanism to replicate in contrast to hover-capable flapping. This is because of the large pitch changes required by hover-capable flapping, in addition to flapping in a single plane like ornithoptic flapping. This distinction has important consequences when one looks at the available literature on flapping flight, wherein,

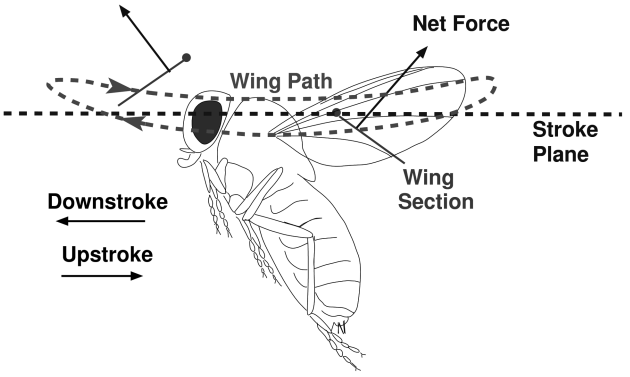

Fig. 2 Insect wing kinematics.

ornithoptic flapping has been studied experimentally to a much greater extent. Literature on hover-capable flapping consists of a considerable amount of research by biologists on the wing kinematics and morphology of actual insects or birds [5–8]. For experimental studies, the problems encountered in making a hover-capable mechanism have been circumvented by making large, slow-moving, dynamically scaled models to mimic insect wing kinematics [9–11].

The flight of insects has intrigued scientists for some time because, at first glance, their flight appears infeasible according to conventional linear, quasi-steady aerodynamic theory [5]. A number of unsteady and nonlinear phenomena have been used to explain the relatively high lift generated by insects. Weis-Fogh's clap-fling hypothesis [12] is one such lift-generating mechanism, but it is limited to a few species of insects and so does not explain the flight of other species. Recent experiments conducted on a dynamically scaled model (Robofly) have shown that insects must take advantage of unsteady aerodynamic phenomena to generate thrusts greater than those predicted by quasi-steady analyses [11]. It must be noted that the thrust refers to the vertical force which balances the insect weight. Figure 2 shows the typical motion of an insect wing. This motion mainly consists of four parts: 1) downstroke, in which the wing translates with a fixed collective pitch angle; 2) near the end of the downstroke the wing supinates so that the blade angle of attack is positive on the upstroke; 3) upstroke; and 4) pronation at the end of the upstroke so that the angle of attack is positive on the downstroke. During the downstroke and upstroke (i.e., the translational phases) high lift is produced because of a leading-edge vortex on the wing [13]. Supination and pronation also produce significant lift from rotational circulation, which is also known as the Kramer effect [14].

The third effect, wake capture, occurs as the wing passes through its own wake, created during the previous half-stroke [11].

The Robofly experiments have shown that the leading-edge vortex is the key to explaining the high thrust generated by insects at low chord Reynolds numbers ($Re \sim 150$). The presence of this attached vortex on the wing has sometimes been explained by the presence of spanwise flow through the vortex core that transports vorticity from inboard to outboard regions of the wing [13,15]. However, Birch et al. [16] have shown that although spanwise flow does exist on the Robofly wings at an Reynolds number of 1400, it is absent at a lower Reynolds number of 120. Ellington and Usherwood [15] also showed that in rotary wing experiments conducted at Reynolds numbers from 10,000 to 50,000, the lift coefficients dropped significantly at higher Reynolds numbers, indicating a weakened leading-edge vortex. Flow visualization studies conducted at a higher Reynolds number ($\sim 19,500$) suggest that the leading-edge vortex is not stable on the wing and that multiple vortices may be generated during the stroke [17]. Thus, the effect of the Reynolds number on the leading-edge vortex is not clearly understood. This is significant because of the fact that flapping wing MAVs operate in the Reynolds number range 10^3–10^5.

Most of the analytical studies on the aerodynamics of hover-capable flapping wings have examined rigid wings [18,19]. Some studies look at ornithoptic or birdlike flapping, that is, flapping without the pronation and supination phases of insectlike flapping. Some are restricted to small disturbances while others are computationally intensive computational fluid dynamics (CFD) simulations. The development and validation of a comprehensive theory for unsteady force generation by hover-capable flapping wings is partly hindered by a lack of experimental data at the chord Reynolds numbers of interest (10^3–10^5).

Analytical studies on the aerodynamics of hover-capable flapping may be classified as quasi-steady models, reduced order models, unsteady vortex lattice models, and CFD, in order of increasing complexity. Quasi-steady analyses do not account for unsteady effects such as the starting vortex or wake capture [20]. Reduced order models use indicial functions to quantify the effects of unsteady wing motion on airloads [21]. DeLaurier [22] developed an aerodynamic model for ornithoptic flapping, which has been applied to the aeroelastic analysis of a large-scale ornithopter [23]. The unsteady vortex lattice method and vortex particle methods have also been applied to flapping wing systems [18,24,25]. CFD methods, which solve the incompressible form of the Navier–Stokes equations, are computationally intensive but they provide a clearer picture of the flow [13,19,26–31]. For comparison with experimental data, these studies rely on model experiments conducted on relatively rigid wings at very low frequencies. For this reason, these analytical models do not account for aeroelastic effects caused by wing bending and twisting under inertial and aerodynamic loading. Some recent studies on aquatic propulsion [32,33] have examined the effects of fish-fin deformations on propulsion using CFD. Bozkurttas et. al. [33] showed improvements in thrust and efficiency, under certain conditions, for airfoils flexible in the chordwise direction.

An important feature of insect wings is that they can elastically deform during flight. Also, unlike birds or bats, insect muscles stop at the wing base so any active control of the wing shape is not likely [34,35]. Passive aeroelastic design is therefore very important for insect wings. The Robofly measurements are based on very low frequencies of motion because the fluid used had a high viscosity. Thus wing bending and passive aeroelastic effects are likely to be very small in the Robofly experiment. A biomimetic flapping–pitching mechanism that operates in air at high flapping frequencies is described by Tarascio and Chopra [36]. In this paper we describe an experimental methodology to measure the thrust generated by wings mounted on this biomimetic flapping mechanism. It must be noted that because of the mechanical complexity involved in replicating insect wing kinematics, the wing motion did not bear resemblance to any natural species. However, the primary features required for hover capability were replicated in the mechanism. The thrust was measured for a number of wing designs at frequencies up to 12 Hz. A novel mechanism with passive pitching of the wing caused by aeroelastic forces was also tested. This paper also describes an aeroelastic analysis for biomimetic flapping wings and its validation with the experimental data presented here. Detailed results of a flow visualization study are documented elsewhere [17]. At a flapping frequency of 11.6 Hz, the Reynolds number based on maximum stroke velocity and mean chord was approximately 15,600 and the reduced frequency was 0.31.

Biomimetic Flapping Wing Test Setup

Flapping Wing Mechanism

The flapping wing test apparatus was a passive-pitch, bistable mechanism capable of emulating insect wing kinematics (Fig. 3). The desired flapping and pitching motion was produced by a Hacker B20 26L brushless motor, which was controlled by a Phoenix PHX-10 sensorless speed controller in combination with a Grand Wing Servo-Tech (GWS) microprocessor precision pulse generator. The motor shaft was rigidly attached to a rotating disk, which in turn was attached to a pin that drove a scotch yoke. The scotch yoke housed ball ends, which were attached to shafts that were free to flap with the motion of the yoke. As the shaft was actively flapped, pitch actuators, which were rigidly attached to the shaft, made contact with Delrin ball ends at the end of each half-stroke. This caused the shaft to pitch and, hence, generated the wing flip at the end of the half-stroke.

The rotation of the shaft or "flip" at the end of each half-stroke was generated by the pitch assembly, which also served to fix the pitch angle of the shaft during the translational phases of the wing motion. The pitch assembly consisted of the main shaft, which was rigidly attached to a cam, and was, in turn, held in place by a Delrin slider and a compression spring (Fig. 4). In combination with the pitch stop, the entire assembly was bistable, in that it allowed the shaft to rest in only two positions. As the pitch actuator made contact with the ball stops at the end of each half-stroke, the cam was forced to rock over to the other stable position, with the compression spring holding it in place until the next rotation.

Force Transducer

Measurement of the flapping and pitching motions, and the small airloads generated by a wing mounted on the flapping mechanism, posed a significant challenge. The inertial and vibratory loads generated by the mechanism made it difficult to obtain meaningful data by mounting the entire mechanism on a load cell. Thus the loads acting on the wings were measured directly at the wing base. To measure these loads, a load cell was designed and built using Entran ESU-025-500 piezoresistive strain gauges. The load cell had a narrow beam cross section on which two strain gauges were mounted to measure the loads in two orthogonal directions (Fig. 5). Each strain gauge was connected in a half-bridge configuration with a dummy

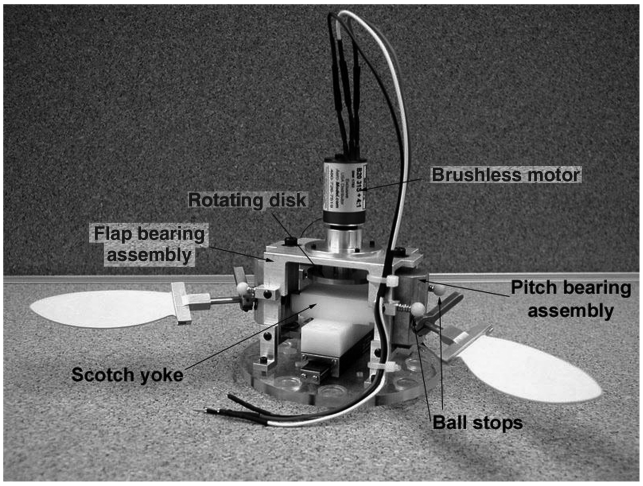

Fig. 3 Flapping wing mechanism (concept by Tarascio and Chopra [36]).

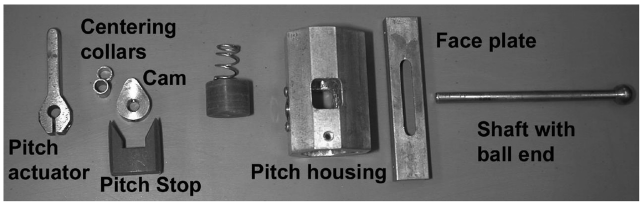

Fig. 4 Components of the pitch assembly.

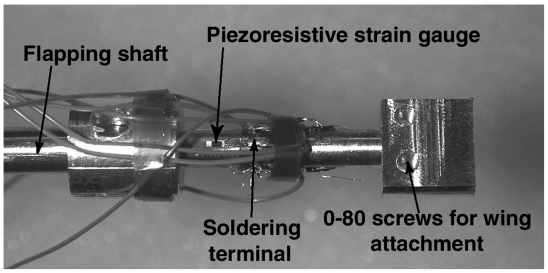

Fig. 5 Load cell.

gauge, which provided temperature compensation. The load cell was mounted at the end of the flapping shaft, with the wing being mounted at the end of the load cell.

Because strain gauges were used on the load cell, only the moment acting at the base of the wing was measured. To convert this moment into an equivalent force, the distance from the wing base at which this force acts must be known. The resultant aerodynamic force on the flapping wings was assumed to act at the point defined by the second moment of wing area [5]. This distance, r_2, was used to determine the forces acting on the wing from the measured moments. These forces were then transformed into vertical and horizontal components using the measured pitch angle. Using two strain gauges separated by some distance, it would be possible to determine the force and the location of the center of pressure. However, the separation between the two gauges could not be increased to the point where accurate data could be obtained. Thus, the use of the distance r_2 was an experimental constraint. The mean aerodynamic thrust was calculated by taking the ensemble average of the vertical force over a number (7–10) of flapping cycles. The mechanism was mounted on the test stand described in the flow visualization section.

Motion Transducers

The load cell measured the forces normal and tangential to the wing chord. To obtain the vertical and horizontal components of these forces, the pitch angle of the shaft was measured. This was done by using a Hall effect sensor in combination with a semicircular disk mounted on the shaft (Fig. 6a). The disk had a tapered flexible magnet in a semicircular slot, with the Hall effect sensor mounted on the pitch housing. The pitching motion of the shaft caused the magnet to move in relation to the Hall effect sensor, producing a change in its output. A flexible magnet was used because it could be easily cut to a taper and molded into the semicircular slot on the disk. In the first generation sensor [37], 10 small magnets were arranged in a semicircle on the disk, which caused the Hall sensor output to change from its maximum positive value to its maximum negative value every 18 deg. This required careful manual application of the calibration curve to convert the raw signal into the pitch angle. However, with the tapered magnet, the calibration was simpler because of the monotonic nature of the Hall sensor output.

In addition to a pitch motion sensor, another Hall sensor was used to measure the flapping motion of the mechanism. In this case, another tapered magnet was mounted on the cross slide of the mechanism, with the Hall sensor fixed to the flap bearing assembly, as shown in Fig. 6b. Because the taper on the magnet was not very smooth, the calibration was nonlinear for both the motion sensors. The flapping motion was used to determine the flapping velocity, which, when multiplied with the horizontal force on the wing, yielded the total aerodynamic and inertial power. When the flapping motion was differentiated to determine the flapping velocity, it was passed through a low pass filter to eliminate the noise introduced by numerical differentiation.

Vacuum Chamber

To quantify the inertial forces acting on the wing, a small vacuum chamber was designed and built using a 16-in. diam, 1/2-in. thick acrylic cylinder (Fig. 7). At the two ends of this cylinder, 1-in. thick acrylic plates were held by screws. The upper plate was fitted with a valve to connect to a vacuum pump. In addition, this plate also had a vacuum gauge and two electrical feedthroughs for connecting the motor, pitch sensor, and force sensor. All vacuum chamber tests were conducted at a gauge pressure of 27 in. of mercury, which corresponds to a 90% vacuum.

Low-Frequency Tests

The thrust generated by aluminum-Mylar wings was measured for a number of stroke and wing parameters. These wings, made from 0.02-in. thick aluminum frames, are shown in Fig. 8. The only difference between wings I and II was the membrane material which made wing II much lighter. It was found that wings I and II produced the same amount of thrust but wing II could attain higher frequencies on the flapping wing mechanism because of its lower mass. In this paper results are presented for wings II and III only. All the results were based on a flapping stroke angle of 80 deg, that is, the flapping angle varied from -40 to $+40$ deg. Each wing was tested at two pitch angles of 30 and 45 deg. A pitch angle of 30 deg implies that the pitch was 30 deg during the downstroke and then changed to -30 deg (150 deg) during the upstroke. Similarly for the 45-deg case, the pitch angle was 45 deg during the downstroke and changed to -45 deg (135 deg) during the upstroke. Figure 9 shows the dimensions of the wings and the root cutout.

In [38], the development of a bending beam load cell with a square cross section was described. This load cell had small cross couplings between the two orthogonal axes of measurement. Figure 10 shows

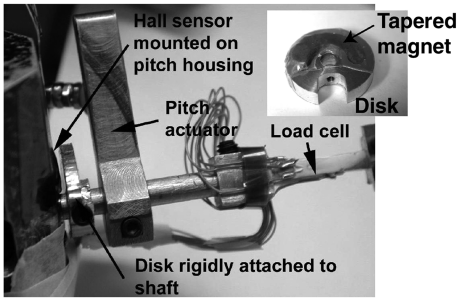

a) Pitch motion sensor

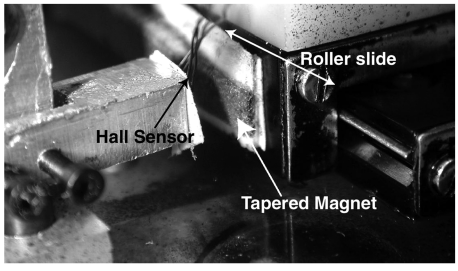

b) Flap motion sensor

Fig. 6 Motion transducers.

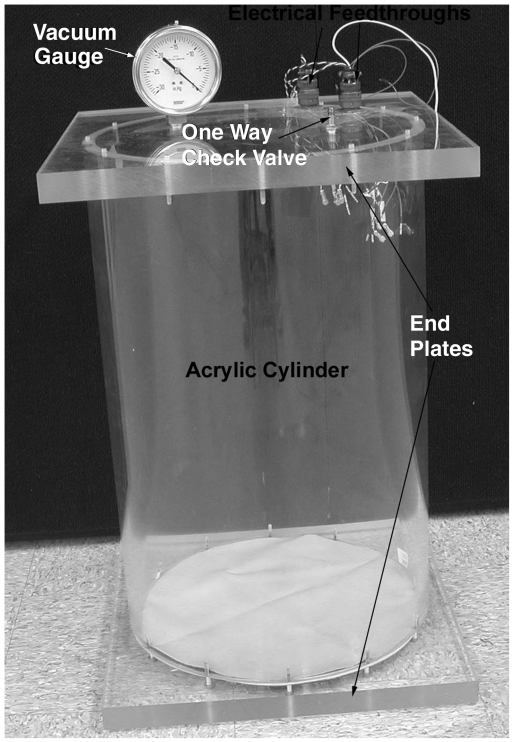

Fig. 7 Vacuum chamber.

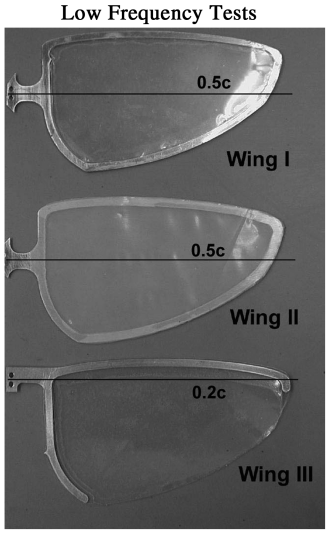

Fig. 8 Scaled-up insect wings.

the thrust generated by wing II when measured with this square cross-section load cell. The thrust measured using this load cell showed a higher-order variation as opposed to the quadratic variation expected. To check whether this discrepancy was caused by the cross coupling present in the load cell, a circular cross-section load cell was designed and built. On a square cross-section load cell, the strain gauges had to be mounted with great precision if spurious surface strains were to be avoided. If the gauge was off center, it could pick up unwanted surface strains that caused the calibration constants to change as the pitch angle of the load cell was varied. On a circular cross section, these spurious strains were minimized. Figure 10 shows the thrust measured using this redesigned load cell. The circular load cell showed a quadratic increase in thrust as the frequency increased. All remaining thrust measurements in this paper were made using the circular cross-section load cell. Although this cross section provided good results, it suffered from the drawback that the strain gauges did not have a flat surface to bond

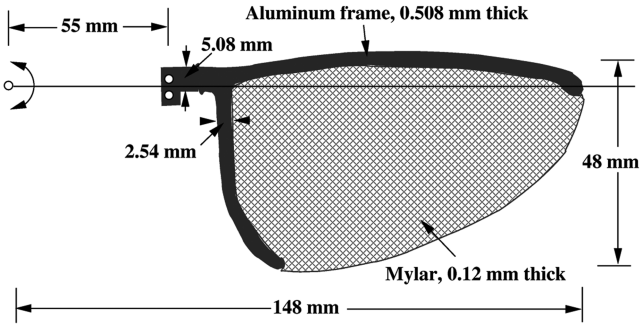

Fig. 9 Schematic of planform showing root cutout.

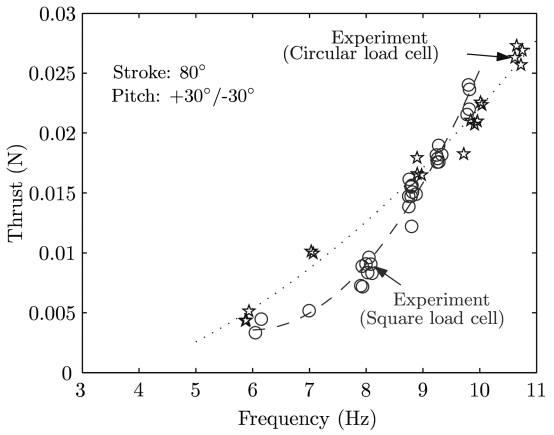

Fig. 10 Effect of change in load cell design on measured thrust.

with. This led to a short useful life of these load cells before the strain gauges had to be replaced, thus increasing the overall testing time.

It must be noted that the mechanism could only be run for a limited time because of the wear and tear caused by its mechanical complexity. Thus, all the tests had to be conducted without damaging the mechanism or the load cell while acquiring as much data as possible. Also, a closer look at the experimental data shows that the mechanism frequency varied slightly between each run (at the same speed controller setting). Accurate error bands could be drawn only if the frequency was steady at a given value. Because of this, all available data were plotted in a scatter plot to show the measurement trends. For wing III, the maximum standard deviation for low-frequency tests was 0.0017 N (3.13% of the mean thrust). At the highest measured thrust, the standard deviation was 0.0027 N (4.48% of the mean thrust).

Figure 11 shows a comparison of the experimental measurements and analytical thrust predictions for the two wings at a pitch angle of 30 deg. Wing III pitched about the 20% chord location, compared to wing II, which pitched about the 50% chord location. This change in pitching axis increased the thrust produced by wing III because it produced more lift from rotational circulation during the pronation and supination phases.

Figure 12 shows the thrust generated by wing II at a pitch angle of 45 deg along with the thrust generated at a pitch angle of 30 deg. At a higher pitch angle, the thrust was expected to increase. However, the experimental results show that the thrust did not change when the pitch angle was increased for wing II. Figure 13 shows similar results for wing III. In this case, however, the experimentally measured thrust did show an increase when the pitch angle was increased to 45 deg.

Inertial forces constituted a large part of the total forces measured using the load cell. To eliminate these inertial loads from the total measured loads, vacuum chamber tests were conducted. When the wing was tested in vacuum, the frequency attained by the mechanism was not the same as the frequency in air at the same motor supply voltage. However, to subtract the inertial forces from the total loads,

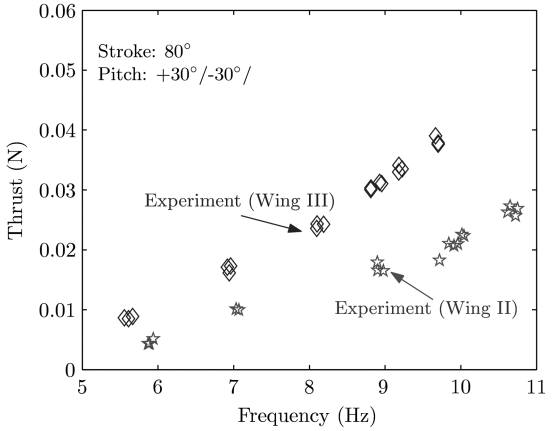

Fig. 11 Comparison of thrust generated by wings II and III.

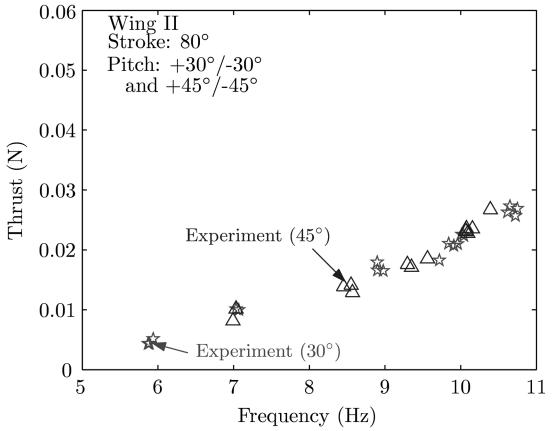

Fig. 12 Effect of wing pitch angle on thrust (wing II).

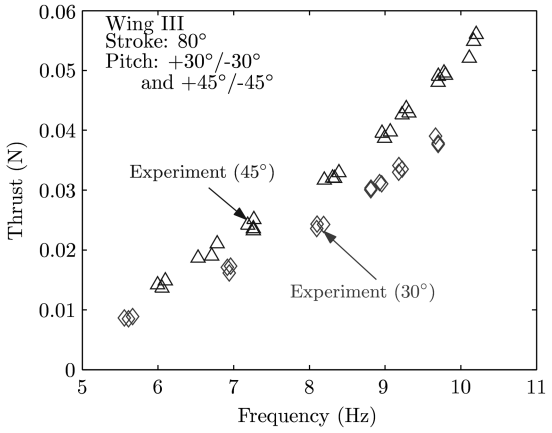

Fig. 13 Effect of wing pitch angle on thrust (wing III).

the test frequencies in air and vacuum must match closely. This was achieved by adjusting the motor supply voltage during the vacuum chamber tests to change the frequency. Figure 14 shows the thrust generated in one flapping cycle by wing II, in air and in vacuum at a frequency close to 10.7 Hz. The frequency for the vacuum test was 10.71 Hz, while the frequency in air was 10.65 Hz. Because these frequencies were slightly different, the results were plotted against nondimensional time in the flapping cycle. Figure 14 also shows the airloads obtained after subtracting the inertial forces from the total forces, and the pitch angle θ, measured both in air and in vacuum. It is evident from this figure that the pitch angle varied slightly in vacuum because of a change in the dynamics of the drive mechanism. Also,

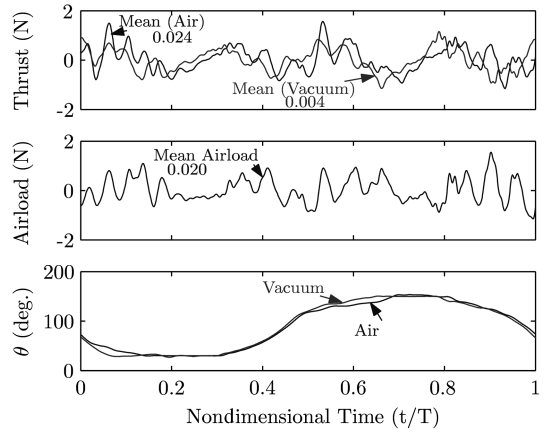

Fig. 14 Airloads obtained by subtracting inertial forces.

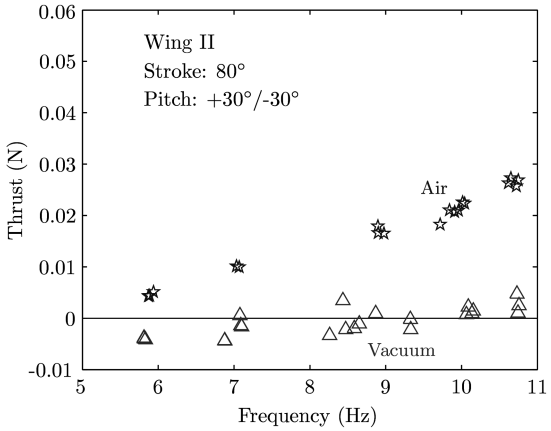

Fig. 15 Thrust measured in air and vacuum for wing II.

the temporal variation of airloads contained frequencies higher than the flapping frequency, which may be caused by the elastic bending and twisting of the wing. The variation in the airloads was expected to be an order of magnitude smaller than the inertial loads. However, the results showed this variation to be of the same order as the combined loads. This may be caused by the variation in the dynamics of the mechanism itself. However, the average thrust measured in vacuum showed that, as expected, wing II generated nearly zero thrust at a pitch angle of 30 deg (Fig. 15). The measurement error in the vacuum chamber data was larger as compared to the measurement error in air. Although the vacuum chamber data did not provide a reliable temporal variation of the airloads, they did increase the confidence level in the thrust measurement methodology using the load cell.

High-Frequency Tests

The low-frequency tests were carried out to a maximum frequency of ∼10.5 Hz. In this section, results are presented for some high-frequency tests carried out on wing III. The wing was tested at a pitch angle of 45 deg because the combination of wing III with 45-deg pitch was found to produce the maximum thrust in the low-frequency tests. Also, for these tests, the flap position was measured in order to calculate the total inertial and aerodynamic power (power = torque × flap velocity). Figure 16 shows the measured thrust and power for wing III up to a frequency of ∼11.6 Hz. The dashed lines show curve fits through the data points. The thrust showed an increase up to a frequency of 10.6 Hz, and then decreased sharply. The frequency range for which these tests were carried out was very small because wing III weighed 1.3 g, which required a lot of power input to the mechanism. It must be noted that the power shown in Fig. 16 was computed from the measured stroke velocity and the measured forces

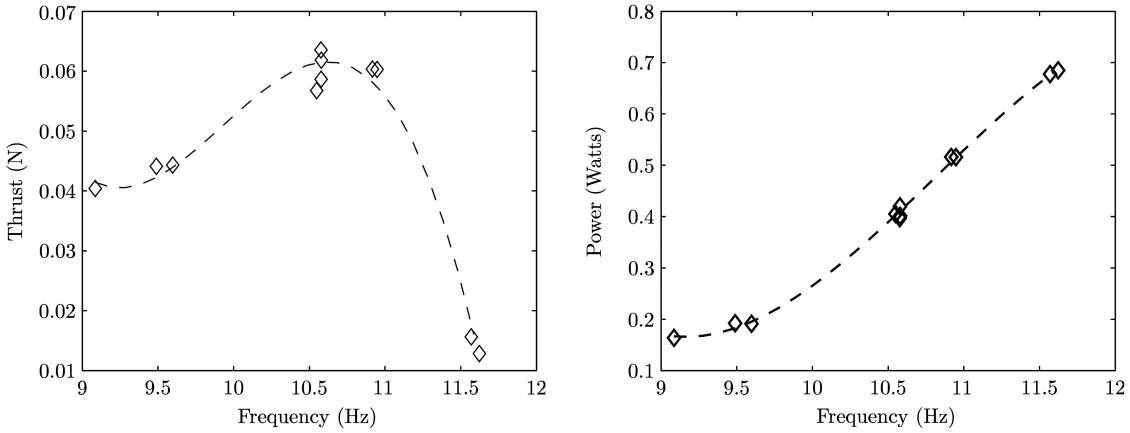

a) Thrust **b) Power**

Fig. 16 Thrust and power measured for wing III at high frequency.

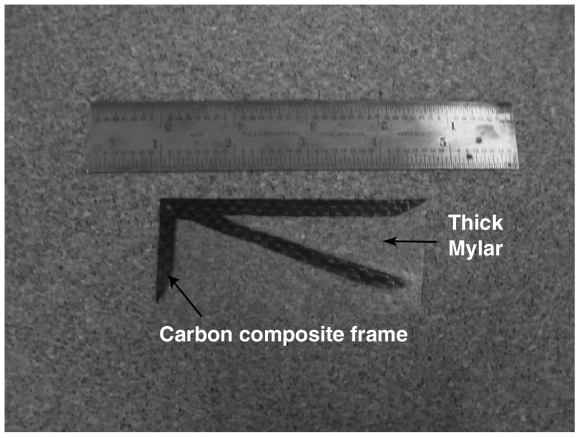

Fig. 17 Wing VII.

at the base of the wing. Therefore, this power includes the aerodynamic and inertial power needed to move the wing at a particular frequency, but does not give any information about the power required by the mechanism as a whole. Without the wing, the mechanism could be run at almost 20 Hz. This indicated that the mass of the wing was preventing the mechanism from moving at high frequency. Also, only a limited amount of data could be acquired because, when the frequency was increased further, the pitch stop (shown in Fig. 4) failed because of the high forces.

Because of the large effect of wing mass on flapping frequency, several lightweight wings were built with composite frames instead of aluminum. Figure 17 shows one such wing with a carbon composite frame covered with a Mylar sheet. Table 1 shows the properties of these wings. All wings with a rectangular planform had the same mean chord as wings II and III. Wings IV, V, and VI were covered with a lightweight film called RC Microlite, which is similar to Monokote widely used by model airplane enthusiasts. Wings VII and VIII used the same frames as wings V and VI, respectively, covered with a Mylar sheet which is stronger and heavier than RC Microlite. All the composite wings were made of rectangular planform because it was easier to cut these shapes out. The first flap frequencies shown in Table 1 were determined from the impulse response of the wings, when mounted on the load cell. These frequencies were the fundamental structural resonance frequencies of the wings.

Figure 18 shows the measured thrust and power for wings IV and V. The thrust and power measured for wing III are also shown on these plots. It is evident from the range of frequencies for each wing that a lower wing mass helped in attaining high frequencies on the mechanism. The lower wing mass also led to lower power as compared to wing III. However, the thrust generated by wings IV and V was much lower than wing III. Also, as with wing III, the thrust attained a maximum value and then decreased with increasing frequency.

Figure 19 shows the thrust and power measured for wings VI and VII. Again, thrust and power for wing III are also plotted for reference. Wing VI was the lightest wing tested but it was also highly flexible. The thrust generated by this wing was very low because it was too flexible to carry any load. Wing VII was built to determine the effect of the skin material on thrust. Wings IV and V used RC Microlite, which although lighter than the Mylar sheet, had many wrinkles on it in addition to being very pliable. In comparison, the Mylar sheet provided a relatively stiff, smooth membrane. Using the Mylar instead of RC Microlite increased the thrust for wing VII by a small amount, although the frequency range was reduced because of the higher mass of the Mylar sheet. A significant increase in the power was also noted. For both wings, the thrust increased and then decreased with increasing frequency. Also, the scatter in thrust measurements increased at high frequency for wings IV and VII.

Passive-Pitch Mechanism

A major concern with the biomimetic mechanism described above was the frequency that the wings could be tested at. This frequency

Table 1 Wing properties

Wing	Planform	Pitching axis	Frame material	Covering material	Mass, g	First flap frequency, Hz
II	Fruit fly	0.5c	Aluminum	Mylar	1.3	35.1
III	Fruit fly	0.2c	Aluminum	Mylar	1.3	32.1
IV	Rectangular	0.1c	Carbon composite	RC Microlite	0.49	24.4
V	Rectangular	0.1c	Carbon composite	RC Microlite	0.65	34.9
VI	Rectangular	0.1c	Fiberglass	RC Microlite	0.39	13.0
VII	Rectangular	0.1c	Carbon composite	Mylar	0.86	34.2
VIII	Rectangular	0.1c	Fiberglass	Mylar	0.61	——
IX	Fruit fly	0.2c	Fiberglass	Mylar	0.58	15.03
X	Rectangular	0.1c	Carbon composite	Mylar	0.68	——

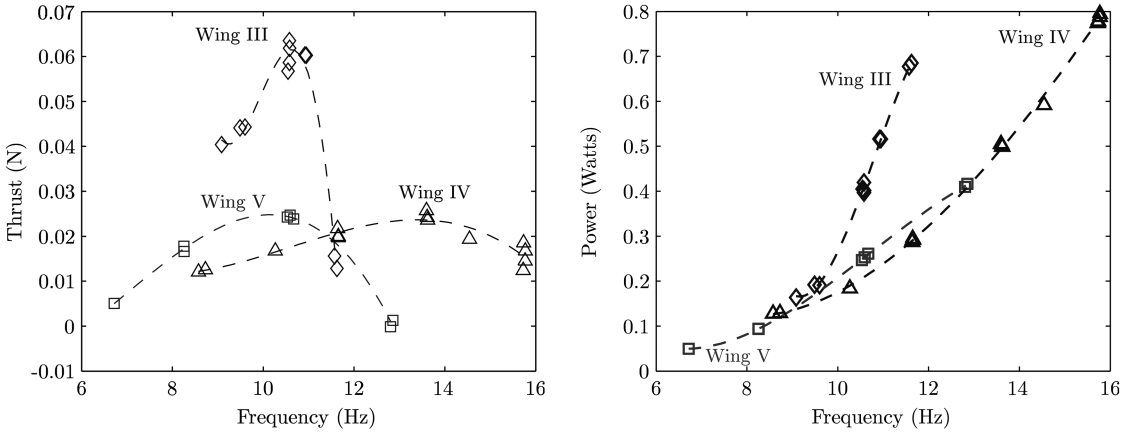

a) Thrust b) Power

Fig. 18 Thrust and power measured for lighter wings at high frequency.

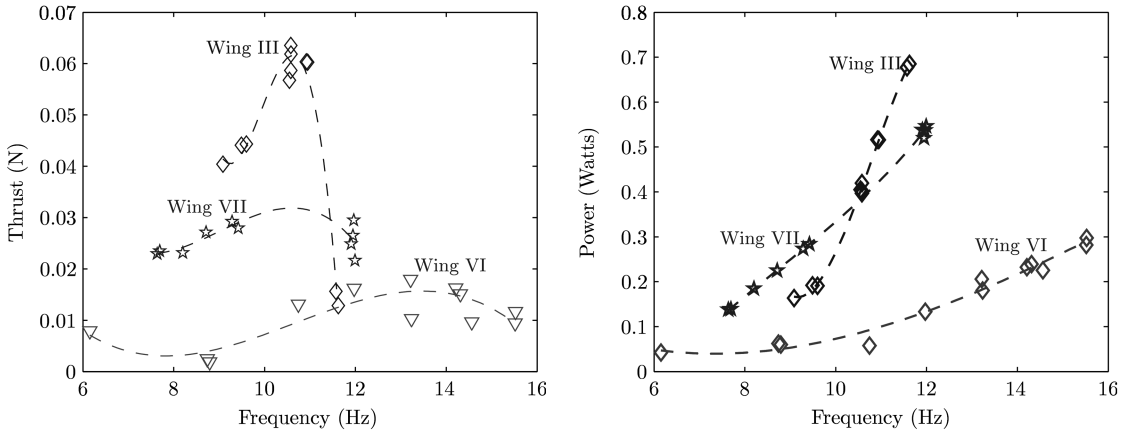

a) Thrust b) Power

Fig. 19 Thrust and power measured for lighter wings at high frequency.

was not only limited because of the wing mass but also because of the pitch actuator hitting the ball ends during the wing flip. Initial tests conducted on a pure flap mechanism with the wing chord held vertical showed high thrust generated by wing VII. This mechanism could be tested at higher frequencies because there was no active pitching of the wing. Based on these results the flapping wing mechanism was modified to include a torsion spring at the base of the wing. This enabled passive pitching of the wing because of the inertial and aerodynamic forces caused by the flapping motion. Figure 20 shows the details of this mechanism. The flapping shaft passed through a set of bearings in the pitch bearing assembly. This enabled the shaft to rotate to any angular position. This rotation was prevented by a torsion spring made from a carbon fiber flexure, which was held rigidly to the shaft. The rotation of the shaft caused the carbon fiber bar to flex, thus providing the torsional stiffness. By moving the shaft-flexure connector further inboard, the torsional stiffness could be increased.

Figure 21 shows the measured thrust and power for two positions of the shaft-flexure connector, one providing a stiff spring and the other a soft spring. Wing VII was used for both tests. Figure 22 shows the minimum and maximum values of the pitch angle variation for both cases. It is evident that the soft torsion spring allowed a larger pitch variation and produced more thrust at a slightly lower power than the stiff spring case. However, even with the spring in the stiff position, the wing could generate approximately 0.09 N of thrust with a pitch variation of just ± 10 deg. This may be caused by the flexibility of the wing itself. To achieve high frequency, and hence high thrust, the wing had to be made lightweight. However, a light wing also became very flexible. This made it very difficult to separate

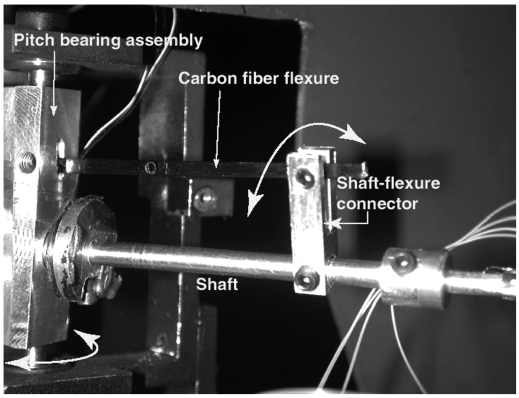

Fig. 20 Passive-pitch mechanism.

the effect of the pitching of the shaft from the torsion of the wing caused by its own flexibility.

Figure 23 shows the measured thrust and power for wings III, VII, and X for various flapping frequencies. Figure 24 shows the corresponding values of minimum and maximum pitch angles. The difference between wings VII and X was that wing X was machined rather than being cut with a blade like wing VII. Thus wing X was lighter than wing VII, and it could attain a higher frequency on the flapping wing mechanism. However, at the same frequency, the pitch angle variation for wing X was smaller than wing VII. This was

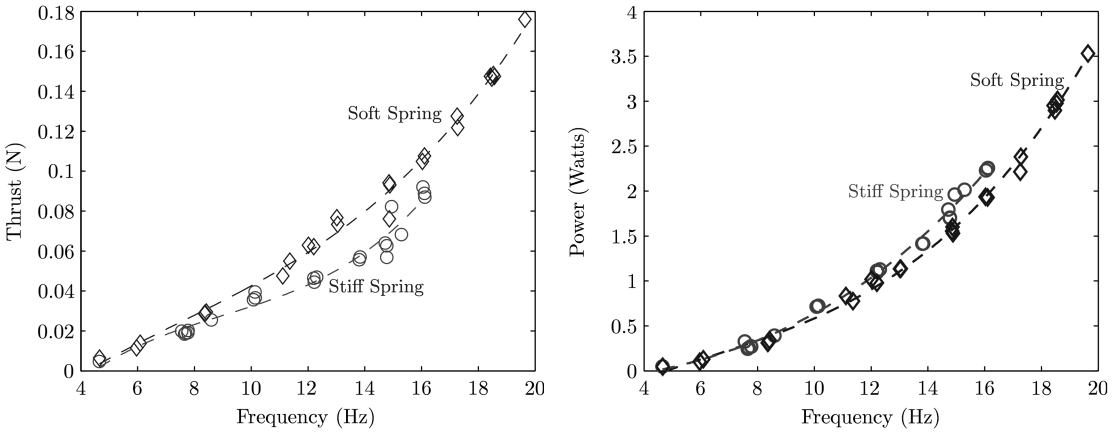

a) Thrust **b) Power**

Fig. 21 Thrust and power measured for passive-pitch mechanism with stiff and soft torsion springs for wing VII.

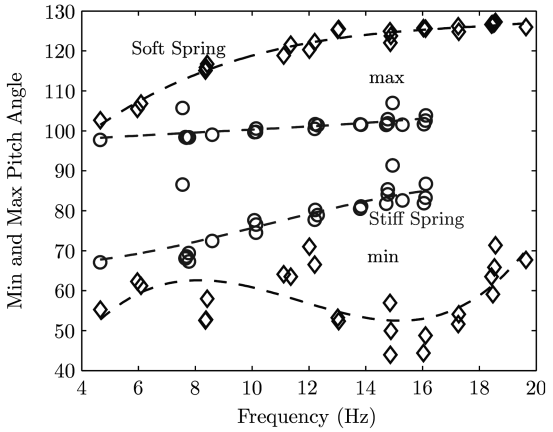

Fig. 22 Minimum and maximum values of pitch variation for stiff and soft springs for wing VII.

reflected in the lower thrust generated by wing X as compared to wing VII. The smaller pitch variation for wing X may be related to its lower mass and altered center of gravity location. The location of the center of gravity behind the wing elastic axis is one of the important parameters for generating a greater pitching motion because of the inertial forces acting on the wing.

Analytical Model

In this section, the structural and aerodynamic analyses used to model the aeroelastic behavior of hover-capable flapping wings are described. Because most insect wings, and the wings used in experiments, are low-aspect ratio wings, plate finite elements were used to model these structures. The approaches available for aerodynamic modeling range from indicial methods based on Wagner and Kussner functions to the computationally intensive unsteady vortex lattice method (UVLM) and CFD analyses. In the present study, for coupling with the structural model, we describe an unsteady aerodynamic model based on indicial functions, because this is the least complex and computationally efficient.

Structural Model

The structural model needs to account for the large overall motions of the wing, which was discretized using plate finite elements, as shown in Fig. 25. The problem of plates as well as arbitrary flexible bodies undergoing large overall motions has been studied before [39–41], although, the method has not been applied to the dynamics of flapping–pitching wings. To obtain accurate predictions of the dynamics of a flexible body undergoing large overall motions, dynamic stiffening must be accounted for in the formulation of the total kinetic energy.

Strain Energy

With the assumption of small deformations, the linear strains for a plate can be written as

$$\{\epsilon\} = \{\epsilon^0\} + z\{\kappa\} \tag{1}$$

where $\{\epsilon^0\}$ is the vector of membrane strains, $\{\kappa\}$ is the vector of curvatures, and z is the coordinate perpendicular to the plane of the

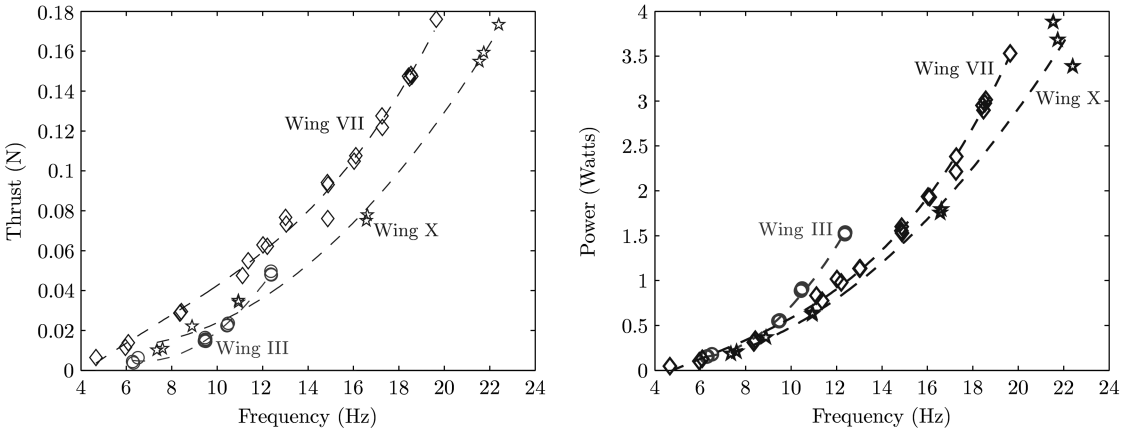

a) Thrust **b) Power**

Fig. 23 Thrust and power measured for passive-pitch mechanism with various wings.

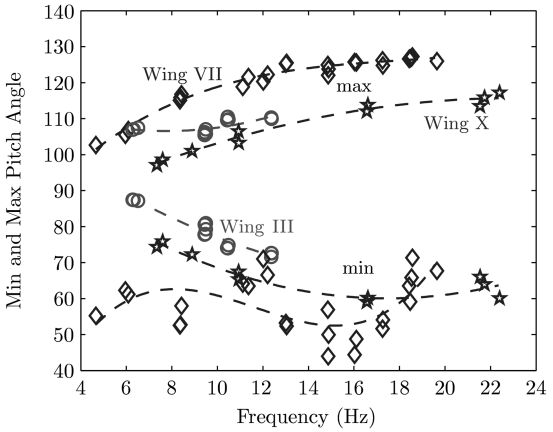

Fig. 24 Minimum and maximum values of pitch variation for various wings mounted on the passive-pitch mechanism.

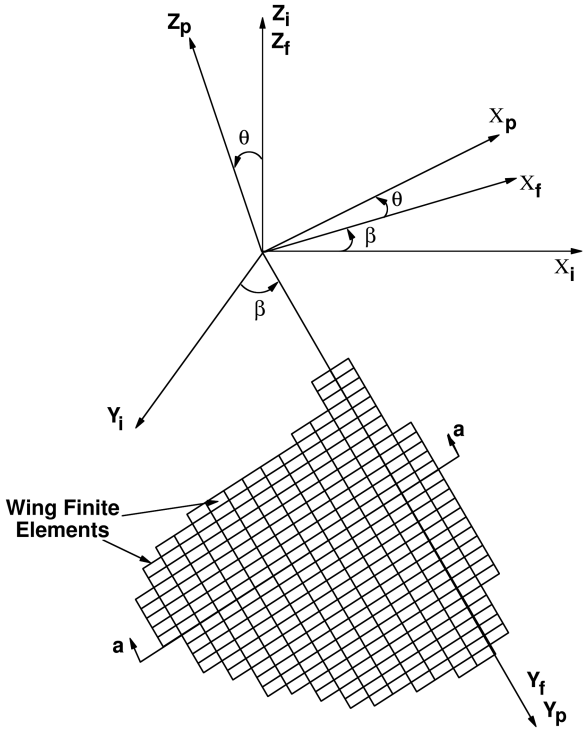

Fig. 25 Reference frames.

plate. Using the material constitutive relation, $\sigma = [Q]\epsilon$, the variation of strain energy can be written as

$$\delta U = \iiint_V \{\delta\epsilon\}^T [Q]\{\epsilon\}\,\mathrm{d}x\,\mathrm{d}y\,\mathrm{d}z \tag{2}$$

The formulation of the structural stiffness and mass matrices for a static composite plate, that is, a wing that is not undergoing flapping or pitching, is well documented [42] and thus will not be detailed here. A 4-node, 24 degree of freedom, conforming plate element is used to model the wing.

Kinetic Energy

Figure 25 shows the reference frames used to describe the motion of the wing. The inertial reference frame X_i, Y_i, Z_i has its origin at the center of rotation. The flapping angle β denotes the rotation of the flapping reference frame X_f, Y_f, Z_f, about the Z_i axis as shown. The wing pitching reference frame X_p, Y_p, Z_p is obtained by rotating the flapping reference frame by the wing pitch angle θ, about the Y_f axis. The relevant orthonormal transformation matrices are

$$\begin{Bmatrix} i_p \\ j_p \\ k_p \end{Bmatrix} = \begin{bmatrix} \cos\theta & 0 & \sin\theta \\ 0 & 1 & 0 \\ -\sin\theta & 0 & \cos\theta \end{bmatrix} \begin{Bmatrix} i_f \\ j_f \\ k_f \end{Bmatrix} = [T_{pf}] \begin{Bmatrix} i_f \\ j_f \\ k_f \end{Bmatrix} \tag{3}$$

$$\begin{Bmatrix} i_f \\ j_f \\ k_f \end{Bmatrix} = \begin{bmatrix} \cos\beta & -\sin\beta & 0 \\ \sin\beta & \cos\beta & 0 \\ 0 & 0 & 1 \end{bmatrix} \begin{Bmatrix} i_i \\ j_i \\ k_i \end{Bmatrix} = [T_{fi}] \begin{Bmatrix} i_i \\ j_i \\ k_i \end{Bmatrix} \tag{4}$$

The position vector of a point on the wing in the pitching frame is given by [39]

$$r_p = \left\{ x_1 - \int_0^{x_1} \frac{1}{2}\left(\frac{\partial w}{\partial x}\right)^2 \mathrm{d}x, y_1 - \int_0^{y_1} \frac{1}{2}\left(\frac{\partial w}{\partial y}\right)^2 \mathrm{d}y, w \right\} \begin{Bmatrix} i_p \\ j_p \\ k_p \end{Bmatrix} \tag{5}$$

The integral terms in the above equation represent the foreshortening effect in the in-plane directions of the wing. These terms must be included to account for the dynamic stiffening of the wing under centrifugal forces. Using the transformation matrices described above, the position vector of a point on the wing can be written in the inertial reference frame, as

$$r_i = \left\{ x_1 - \int_0^{x_1} \frac{1}{2}\left(\frac{\partial w}{\partial x}\right)^2 \mathrm{d}x, y_1 - \int_0^{y_1} \frac{1}{2}\left(\frac{\partial w}{\partial y}\right)^2 \mathrm{d}y, w \right\} [T_{pf}][T_{fi}] \begin{Bmatrix} i_i \\ j_i \\ k_i \end{Bmatrix} \tag{6}$$

Thus, the velocity of a point on the wing can be found using the following equation:

$$V = \frac{\mathrm{d}r_i}{\mathrm{d}t} \tag{7}$$

The variation of the kinetic energy is then obtained from the following relation:

$$\delta KE = \iiint_V V \cdot \delta V\,\mathrm{d}x\,\mathrm{d}y\,\mathrm{d}z \tag{8}$$

Using this functional along with the wing strain energy functional and using Hamilton's principle, the equations of motion for a plate undergoing large flapping and pitching motions can be obtained. The dynamic response of a static wing is governed by the following equation:

$$M\ddot{q} + Kq = 0 \tag{9}$$

The eigenvalues and eigenvectors of this system are denoted by Λ and Φ. When the wing motion is prescribed, that is, $\theta(t)$ and $\beta(t)$ are known as a function of time, the equations of motion can be written as

$$M\ddot{q} + C\dot{q} + K(\theta(t), \beta(t))q = F(\theta(t), \beta(t)) \tag{10}$$

where the stiffness matrix K is now a function of the prescribed overall base motions. The modal matrix Φ for the static case was used to reduce the size of the above system, by retaining the first "m" modes in the analysis. The resulting system of equations was integrated to obtain the motion of the wing. Once the motion of the wing was known, the bending moment at the base of the wing could be obtained by a surface integral of the inertial loads acting on the wing.

Aerodynamic Model

The aerodynamic analysis is a blade element formulation, based on the assumption that the aerodynamic forces acting on a flapping–pitching wing can be broken down into a number of components which are accounted for separately and then added to obtain the total force. Determining the validity of this assumption will require comparisons with more detailed analyses. However, this analysis serves as a first step. The effects of wing elastic deformations were

also accounted for in the analysis. The following components contribute to the total aerodynamic force:

1) The translational and rotational circulation based on thin airfoil theory, with wing elasticity effects included.

2) The effect of a leading-edge vortex on the wing, determined by using Polhamus's leading-edge suction analogy for delta wings at high angles of attack [21,43].

3) Noncirculatory forces based on thin airfoil theory [44].

4) The effect of the starting vortex on the translational and rotational circulation. This was accounted for by using the Wagner function.

5) The effect of the shed wake and a tip vortex, accounted for by using the Kussner function. The induced inflow velocity was determined based on momentum considerations.

Figure 26 shows the leading-edge vortex and the structure of the wake at one radial location along the wing. Figure 27 shows the flow velocities at this radial location. Using these velocities, the formulation of [44] may be extended to include elastic effects as shown below. In thin airfoil theory, the problem reduces to the determination of a circulation distribution γ along the chord, as governed by the following integral equation:

$$\frac{1}{2\pi}\int_0^c \frac{\gamma(\xi)}{(x-\xi)}\,\mathrm{d}\xi = V_n + \dot{\theta}(x-ac) - \dot{w}(x) - V_p\frac{\partial w}{\partial x} \tag{11}$$

It must be noted that, because the normal and parallel velocities were used in the above equation, there is no small angle assumption involved. The circulation distribution γ can be determined by using the transformation $\xi = c/2(1-\cos\phi)$ and expressing $\gamma(\xi)$ in terms of a Fourier series in ϕ [44],

$$\gamma(\phi) = 2V\left(A_0\frac{1+\cos\phi}{\sin\phi} + \sum_{n=1}^{\infty} A_n \sin n\phi\right) \tag{12}$$

Substituting Eq. (12) in Eq. (11), the Fourier series coefficients can be determined as

$$A_0 = \frac{V_n}{V} + \frac{c\dot{\theta}}{V}\left(\frac{1}{2}-a\right) - \frac{1}{\pi V}\int_0^\pi \dot{w}\,\mathrm{d}\phi - \frac{V_p}{\pi V}\int_0^\pi \frac{\partial w}{\partial x}\,\mathrm{d}\phi \tag{13}$$

$$A_1 = \frac{1}{2}\frac{c\dot{\theta}}{V} + \frac{2}{\pi V}\int_0^\pi \dot{w}\cos\phi\,\mathrm{d}\phi - \frac{2V_p}{\pi V}\int_0^\pi \frac{\partial w}{\partial x}\cos\phi\,\mathrm{d}\phi \tag{14}$$

$$A_n = \frac{2}{\pi V}\int_0^\pi \dot{w}\cos n\phi\,\mathrm{d}\phi - \frac{2V_p}{\pi V}\int_0^\pi \frac{\partial w}{\partial x}\cos n\phi\,\mathrm{d}\phi \tag{15}$$

The total circulation can be obtained by integrating $\gamma(\phi)$ along the chord,

$$\Gamma(t) = \pi V c\left(A_0(t) + \frac{A_1(t)}{2}\right) \tag{16}$$

Thus the horizontal and vertical circulatory forces, without any unsteady effects, can be determined as

$$F_v^c(t) = \rho V_h(t)\Gamma(t) \tag{17}$$

$$F_h^c(t) = \rho V_v(t)\Gamma(t) \tag{18}$$

Apparent Mass

For a flapping–pitching wing, the forces exerted by the fluid because of its acceleration and deceleration must also be accounted for. Using the unsteady Bernoulli equation, the pressure difference along the chord, caused by this added mass effect, can be written as [44]

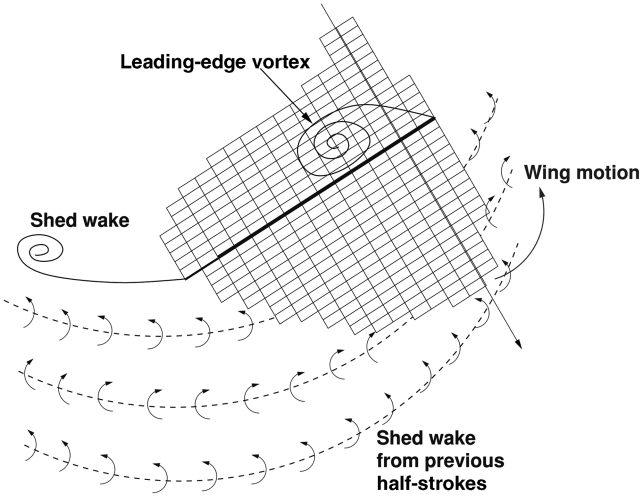

Fig. 26 Wake structure at one station along the span.

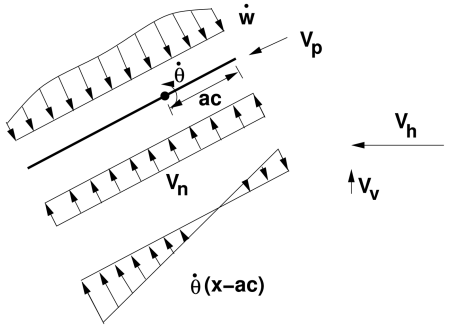

Fig. 27 Flow velocities.

$$\Delta p^{\mathrm{nc}} = \frac{\partial}{\partial t}\int_0^x \gamma(\xi,t)\,\mathrm{d}\xi = \frac{\partial}{\partial t}\Gamma(x,t) \tag{19}$$

Thus, the force normal to the wing caused by the added mass or noncirculatory effect is

$$F_n^{\mathrm{nc}} = \rho\int_0^c \frac{\partial}{\partial t}\Gamma(x,t)\,\mathrm{d}x = \frac{\rho c^2}{2}\left[\frac{3}{2}\pi\frac{\partial}{\partial t}(A_0(t)V(t)) + \frac{\pi}{2}\frac{\partial}{\partial t}(A_1(t)V(t)) \frac{\pi}{4}\frac{\partial}{\partial t}(A_2(t)V(t))\right] \tag{20}$$

Leading-Edge Suction

The suction force generated by the presence of a leading-edge vortex on top of the wing was modeled using an approach similar to that used for modeling the vortices that occur on delta wings at high angles of attack [43,45,46]. This method assumes that, at high angles of attack, the leading-edge suction force on an airfoil is rotated by 90 deg and acts in the same way as the suction force that would be generated by the presence of a vortex on top of the wing. The normal force is thus given by

$$F_n^{\mathrm{pol}}(t) = \rho\Gamma(t)V_h(t)\sin\alpha \tag{21}$$

where $\Gamma(t)$ is given by Eq. (16).

Unsteady Effects

The effect of the starting vortex on the buildup of circulation was accounted for by using the Wagner function ϕ_w. Using this function, the effect of the starting vortex on the forces given by Eq. (18), can be written using the Duhamel integral as

$$F_v^c(t) = \rho V_h(0)\Gamma(0)\phi_w(t) + \rho V_h(t)\int_0^t \frac{\mathrm{d}\Gamma}{\mathrm{d}\sigma}\phi_w(t-\sigma)\,\mathrm{d}\sigma \quad (22)$$

$$F_h^c(t) = \rho V_v(0)\Gamma(0)\phi_w(t) + \rho V_v(t)\int_0^t \frac{\mathrm{d}\Gamma}{\mathrm{d}\sigma}\phi_w(t-\sigma)\,\mathrm{d}\sigma \quad (23)$$

The effect of the shed wake from the previous flapping strokes was accounted for by using the Kussner gust response function ψ_k. The shed vorticity strength was computed using the following equation:

$$\gamma_w(x,t) = -\frac{1}{V(t)}\frac{\mathrm{d}\Gamma(t)}{\mathrm{d}t} \quad (24)$$

At the end of each stroke, this vorticity distribution was assumed to convect below the wing by a distance $v_i T/2$. With the vorticity distribution below the wing determined, the gust velocity w_g generated by this distribution was used in a Duhamel integral to determine its effect on the forces acting on the wing,

$$F_v^k = \rho V_h(t)\int_0^t \frac{\mathrm{d}\Gamma}{\mathrm{d}w_g}\frac{\mathrm{d}w_g}{\mathrm{d}\sigma}\psi_k(t-\sigma)\,\mathrm{d}\sigma \quad (25)$$

$$F_h^k = \rho V_v(t)\int_0^t \frac{\mathrm{d}\Gamma}{\mathrm{d}w_g}\frac{\mathrm{d}w_g}{\mathrm{d}\sigma}\psi_k(t-\sigma)\,\mathrm{d}\sigma \quad (26)$$

A tip vortex was also modeled based on the assumption that all the vorticity beyond the point of maximum circulation, along the wing span, rolls up into a tip vortex [47]. This tip vortex also convects downward based on the induced inflow velocity and affects the gust velocity seen by the wing. Each blade element was independent of the other blade elements, such that the shed wake of a blade element and the tip vortex were used to determine the gust velocity. Because a root cutout was present, a root vortex was also expected. However, because of low wing velocity at the root we assumed that the strength of this vortex was negligible. Because the geometry of the shed vortices and the tip vortex was nonplanar, the three-dimensional Biot–Savart law was used to determine the gust velocity.

Elastic Effects

In this section, the procedure to account for the elastic terms in Eq. (15) is described. To illustrate this, consider the elastic part of the coefficient A_0,

$$A_0^{\mathrm{el}} = -\frac{1}{\pi V}\int_0^\pi \dot{w}\,\mathrm{d}\phi - \frac{V_p}{\pi V}\int_0^\pi \frac{\partial w}{\partial x}\,\mathrm{d}\phi \quad (27)$$

Let $b^p(x)$ be the vector of modal deflections for the pth structural mode at the cross section shown in Fig. 27. Similarly, let $b'^p(x)$ be the vector of modal slopes with respect to x. The structural deformations across the chord at this station can then be written as

$$\dot{w}(x,t) = \sum_{p=1}^{N_m} \dot{q}_p(t)b^p(x) \quad (28)$$

$$\frac{\partial w}{\partial x}(x,t) = \sum_{p=1}^{N_m} q_p(t)b'^p(x) \quad (29)$$

where $q_p(t)$ represents the generalized coordinates and N_m is the number of structural modes retained in the analysis. Substituting the above equations into Eq. (27) we get

$$A_0^{\mathrm{el}} = -\frac{1}{\pi V}\sum_{p=1}^{N_m}\dot{q}_p(t)B_0^p - \frac{V_p}{\pi V}\sum_{p=1}^{N_m}\dot{q}_p(t)B_0'^p \quad (30)$$

where B_0^p and $B_0'^p$ are given by

$$B_n^p = \int_0^\pi b^p(x)\cos n\phi\,\mathrm{d}\phi \quad (31)$$

$$B_n'^p = \int_0^\pi b'^p(x)\cos n\phi\,\mathrm{d}\phi \quad (32)$$

with $n = 0$. Thus the dependence of the Fourier coefficients on the chordwise deformation is accounted for by the aerodynamic coefficients B_n^p and $B_n'^p$, which can be determined from the wing mode shapes a priori. Similarly, the other Fourier coefficients can be written as

$$A_1 = \frac{2}{\pi V}\sum_{p=1}^{N_m}\dot{q}_p(t)B_1^p - \frac{2V_p}{\pi V}\sum_{p=1}^{N_m}q_p(t)B_1'^p \quad (33)$$

$$A_n = \frac{2}{\pi V}\sum_{p=1}^{N_m}\dot{q}_p(t)B_n^p - \frac{2V_p}{\pi V}\sum_{p=1}^{N_m}q_p(t)B_n'^p \quad (34)$$

Induced Inflow Velocity

To determine the induced inflow velocity v_i, an iterative scheme was employed. The total thrust produced by the flapping–pitching wing was computed as the sum of all the above components. The inflow velocity was obtained from the following equation which is based on momentum considerations:

$$v_i = \sqrt{\frac{T_{\mathrm{total}}}{\rho\Phi R^2}} \quad (35)$$

where R is the total wing span and Φ is the wing stroke angle. The computation of forces and inflow velocity was repeated until the inflow converged.

Model Validation

Structural Model

To validate the structural model, the spin-up motion of a cantilevered plate was studied. The wing tip deflection shows very good correlation with the results of [41], as shown in Fig. 28. The structural model was also validated experimentally for a rectangular aluminum plate undergoing pure flapping motion. To accurately predict the bending moment at the base of the wing, an accurate measurement of the flapping acceleration was of prime importance. The validation of the structural model for an aluminum-Mylar wing undergoing combined flapping and pitching is described in the next section.

Aerodynamic Model

To validate the aerodynamic model, results were compared with experimental data for the Robofly [20]. Because the Robofly has stiff wings that flap at very low frequencies, elastic deformations of its wings were expected to be small. This made it ideal for validating the aerodynamic model without any elastic effects. Figure 29 shows the flap and pitch velocities prescribed in the experiment. These were used as inputs to the present analysis. Figure 30 shows the total aerodynamic force predicted by the analysis as a function of time during the flapping cycle. The dashed line represents experimental data from [20]. The peak occurring just before the end of the downstroke was caused by three effects, namely, the translatory circulation, rotational circulation, and the apparent mass effect. A significant contribution came from the translatory circulation, even though the pitch angle was much larger than 45 deg at this point. The reason for this lies in the ideal translatory lift coefficient from Eqs. (16) and (17). This coefficient is given by

$$C_l^{\mathrm{ideal}} = 2\pi\sin\alpha \quad (36)$$

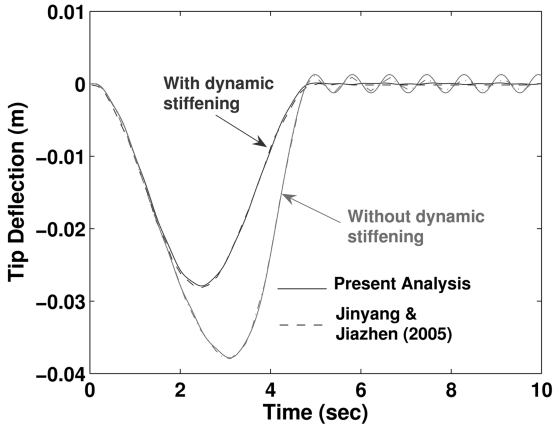

Fig. 28 Tip deflection for spin-up motion of a rectangular plate.

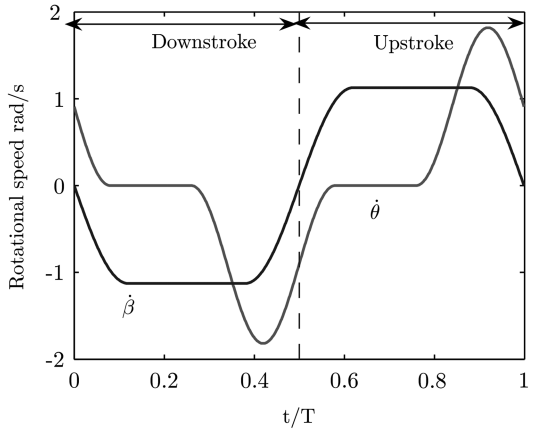

Fig. 29 Input velocities for Robofly kinematics.

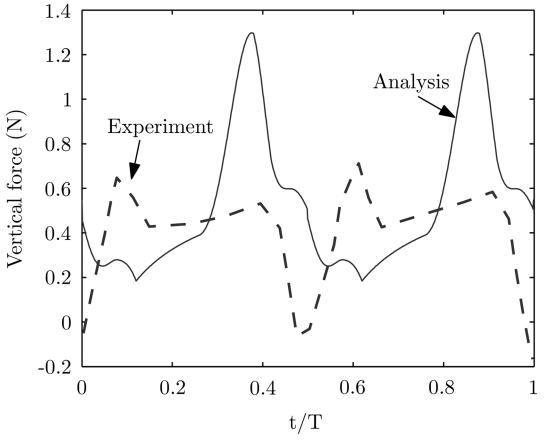

Fig. 30 Total vertical force with ideal C_l.

Figure 31 shows this ideal C_l plotted against the experimental values reported in [11]. It is clear from this figure that, unlike the experimental C_l, the ideal C_l does not show any stall as the pitch angle increases beyond 45 deg. This leads to the overprediction of thrust near the end of the downstroke and upstroke, as seen in Fig. 32. To account for this, the aerodynamic model was modified by using the experimental C_l and C_d values to determine the circulation generated by the translational motion of the wing. Figure 32 shows the vertical force computed using this modified model. It is evident that the model with experimental C_l can predict the aerodynamic forces better than the model with ideal C_l. It must be noted that the experimental force coefficients were obtained by accelerating the

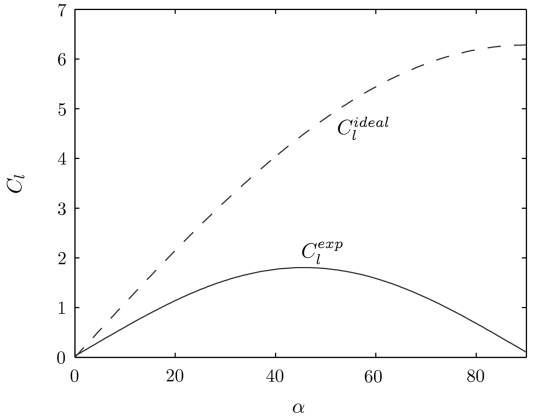

Fig. 31 Ideal C_l compared with experimental C_l.

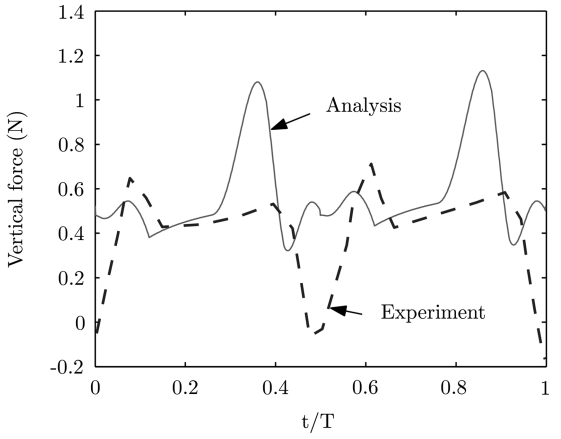

Fig. 32 Total vertical force with experimental C_l.

Robofly wing to a constant velocity at different pitch angles and measuring the forces once the transients disappeared. Thus, these tests were three dimensional in nature. However, this was the only data available for the range of pitch angles needed. Moreover, Wang et al. obtained the same coefficients from a two-dimensional computation [48]. The experimental lift and drag coefficients were used to obtain further results reported in this paper.

Figure 33 shows the breakup of the total vertical force into its individual components. There are several interesting features evident from this figure. First, the force peak at the beginning of each half-stroke is because of noncirculatory effects. Secondly, the slow rise in the force during the middle of each half-stroke is caused by a delayed buildup of circulation that is captured by the Wagner effect. Third, the leading-edge vortex adds to the total thrust during the translatory part of each half-stroke, although this effect is negated to some extent by the shed wake from previous half-strokes, which is accounted for by the Kussner function. The small peak in the circulatory force near the end of each half-stroke is caused by an increase in rotational circulation. It is evident that the discrepancy between experiment and analysis at the end of each half-stroke is caused by the noncirculatory force. Figure 34 shows the comparison between experiment and analysis without the noncirculatory effect. This shows an improvement in the agreement between the analysis and experiment.

At this point, it is pertinent to mention that, in the experiments conducted on the Robofly, the contribution of wing mass acceleration and gravity were removed by using a dummy inertial wing ([11], p. 1960). What is unclear is the way in which this subtraction of inertial effects, using a dummy inertial wing, affected the noncirculatory forces measured on the real wing. Dickinson et al. [11] state that the experiments were repeated for a kinematic pattern with and without a flat stroke plane as shown in Fig. 35. In both cases, the force peak at the beginning of the half-stroke was present. However, the authors use this fact to eliminate noncirculatory forces

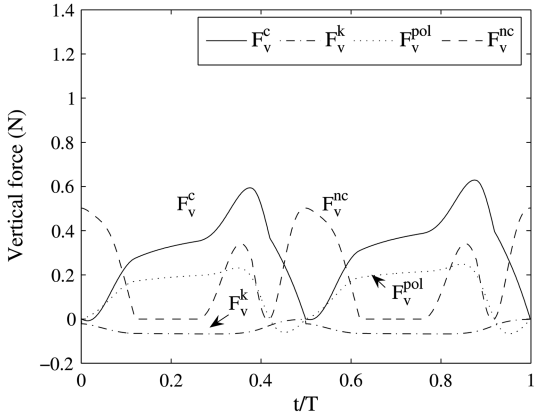

Fig. 33 Components of the total vertical force. F_v^c: circulatory (with Wagner effect); F_v^{pol}: leading-edge suction; F_v^{nc}: noncirculatory; F_v^k: Kussner effect.

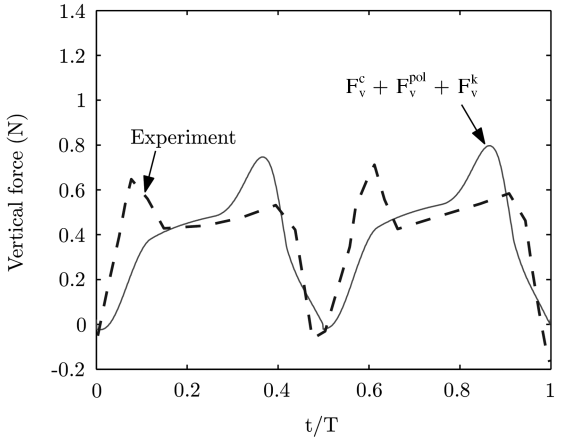

Fig. 34 Vertical force without noncirculatory effects.

as the cause of this force peak, by stating that, for a flat stroke plane, noncirculatory forces cannot contaminate the measurement of the vertical force. This is an erroneous assumption because the noncirculatory force acts perpendicular to the wing, and thus, for a wing held at a large pitch angle, it would affect both the horizontal and vertical forces. Based on this assumption, the force peak at the start of each half-stroke has been entirely attributed to wake capture, with no contribution from noncirculatory effects. However, our predictions indicate that this force peak can be explained, at least in part, by the noncirculatory forces.

Figure 36 shows a comparison of the computed horizontal force (i.e., drag) with the horizontal force measured on the Robofly. During the translatory phase of the motion, the analysis agreed closely with experiment. However, the force peaks at the beginning and end of each half-stroke were not captured very well. These peaks were also caused by noncirculatory effects. Figure 32 shows an instantaneous rise in the vertical force when the wing began its acceleration. Figure 36 shows that the measured increase in drag, near the end of each half-stroke, was slower than that predicted by the analysis. This indicated that compressibility effects may need to be included in the computation of the noncirculatory forces, because compressibility effects may be present when the reduced frequency is high [47].

Results and Discussion

The thrust generated by a number of highly flexible and lightweight wings, undergoing a biomimetic flapping–pitching motion, was measured as reported in the first part of this paper. The high flexibility of these wings makes them ideal candidates for comparison with the analysis described here. In this section, the aerodynamic and structural analyses validated above were used to

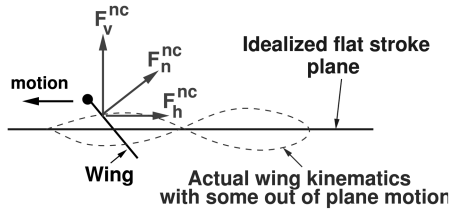

Fig. 35 Actual and idealized stroke planes and the noncirculatory force.

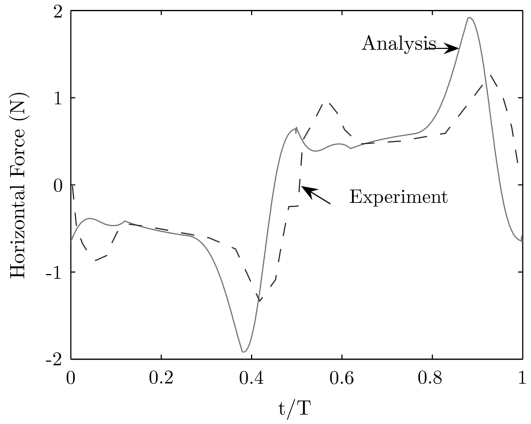

Fig. 36 Total horizontal force.

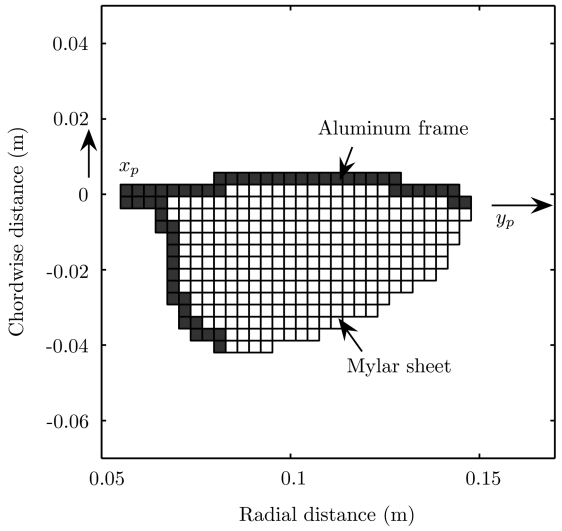

Fig. 37 Finite element grid for wing III.

predict the mean thrust measured on these biomimetic flapping–pitching wings.

Wing Grids

Figures 37 and 38 show the finite element grid used to discretize two of the lightweight wings tested on the biomimetic mechanism. The frames of these wings were made from aluminum. This frame was then covered with a lightweight but sturdy Mylar sheet. From an aerodynamic standpoint, wings II and III were different because of the location of their pitching axes. This axis is defined by the line $x_p = 0$ in Figs. 37 and 38. Wing III pitched about its 20% chord location while wing II pitched about its 50% chord location. The following material properties were used for aluminum: Young's modulus $E = 60$ GPa, mass density $\rho = 2400$ Kg/m^3, Poisson's ratio $\nu = 0.33$, and thickness $t = 5.08 \times 10^{-4}$ m. The material properties used for Mylar were $E = 7$ GPa, $\rho = 1250$ Kg/m^3, $\nu = 0.25$, and $t = 1.04 \times 10^{-4}$ m. The wing grid density was chosen

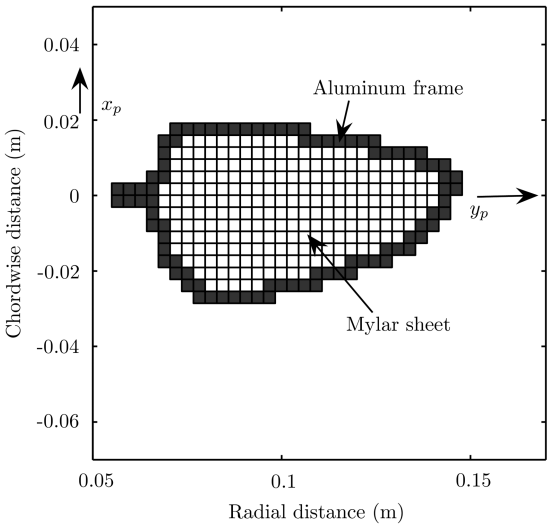

Fig. 38 Finite element grid for Wing II.

to accurately model the aluminum frame width. To check convergence, it was ensured that the bending moment did not change when a higher density grid was used.

Bending Moment Comparison

The bending moment measured from a combined flapping–pitching motion of wings II and III was compared with the bending moment predicted by the analysis. An important observation from our validation of the structural model was the need for an accurate measurement of the flapping acceleration. This is because the accelerations directly affect the inertial loads acting on the wing, which, in turn, affect the measured bending moment. However, in the tests reported in the Introduction of this paper, only the pitch position was measured. For later tests, a flap position sensor was also introduced. But the analysis required position, velocity, and acceleration, for the flapping and pitching motions, as inputs. Numerical differentiation of the measured position introduced significant errors in the computed velocities and accelerations. To alleviate this problem, a Fourier series was fit to the measured flapping and pitch positions, as shown in Fig. 39. The coefficients of this Fourier series were then used to determine the approximate velocity and acceleration. This type of motion is henceforth referred to as approximated motion. Figure 40 shows comparisons between the measured and predicted bending moments for wing III at various frequencies. These frequencies represent the higher range of all frequencies at which test data were available. The input motions for the analysis were approximated from the measured flapping and pitch positions as described previously. It can be seen from this figure that, even with approximate flapping and pitching accelerations, the analysis could predict the bending moment satisfactorily at the lower frequencies. At 10.96 Hz, there was some overprediction of the bending moment. However, at 11.6 Hz, the analysis significantly overpredicted the bending moment. Because a geometrically linear structural model was used, this may be part of the reason for the overprediction. However, the approximation of the accelerations also played a significant role. To illustrate this, the bending moment was recomputed at a frequency of 11.6 Hz with a smooth motion used as an input to the analysis. This smooth motion is compared with the approximated motion in Fig. 41. The bending moment predicted by the analysis at a flapping frequency of 11.6 Hz, using this smooth motion, is shown in Fig. 42. Although there was a significant error, especially in phase, between the measured and predicted values, the peak-to-peak variation showed significant improvement over the prediction using the approximate motion. This underscores the need for an accurate measurement of the flapping and pitching accelerations. The discrepancy in bending moment prediction at high frequency is discussed further in a subsequent section.

Uncoupled Analysis

There is some experimental evidence to suggest that wing bending in hovering insects is predominantly caused by inertial forces alone [49], with aerodynamic forces being an order of magnitude smaller than the inertial loads. Based on this assumption, an uncoupled analysis was carried out. In this analysis, the wing deformations were

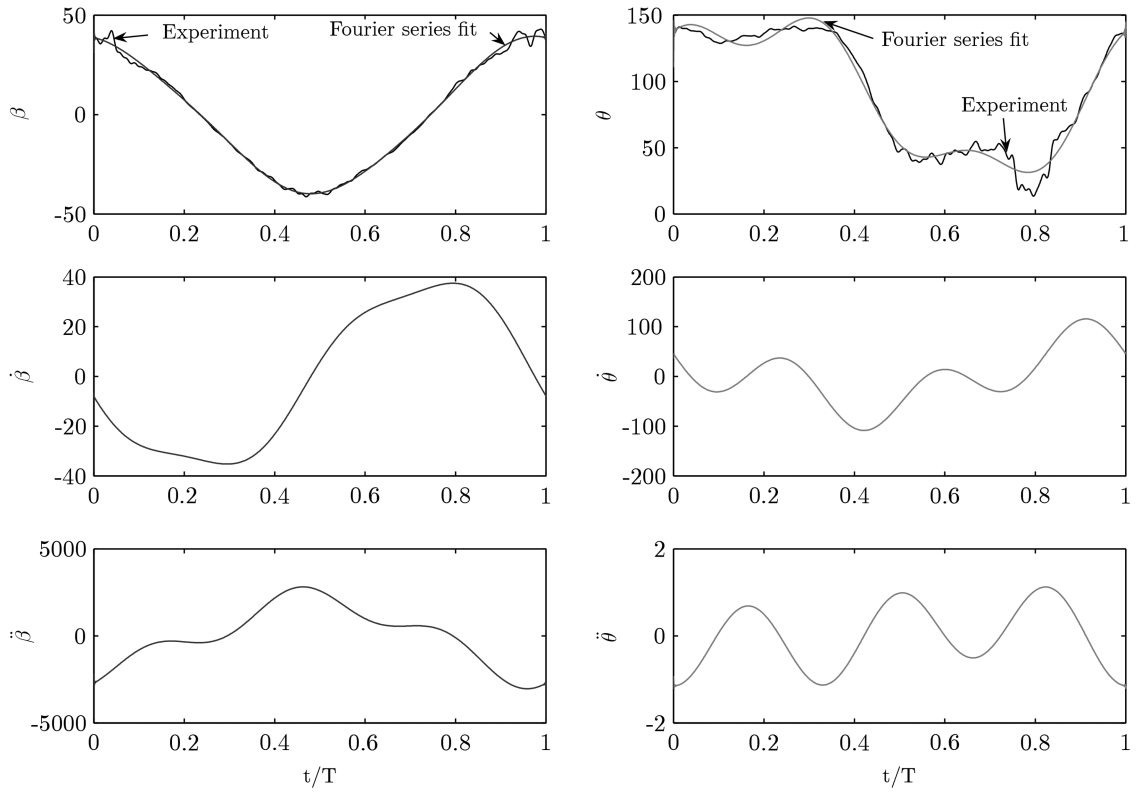

Fig. 39 Position, velocity, and accelerations used as inputs for the analysis.

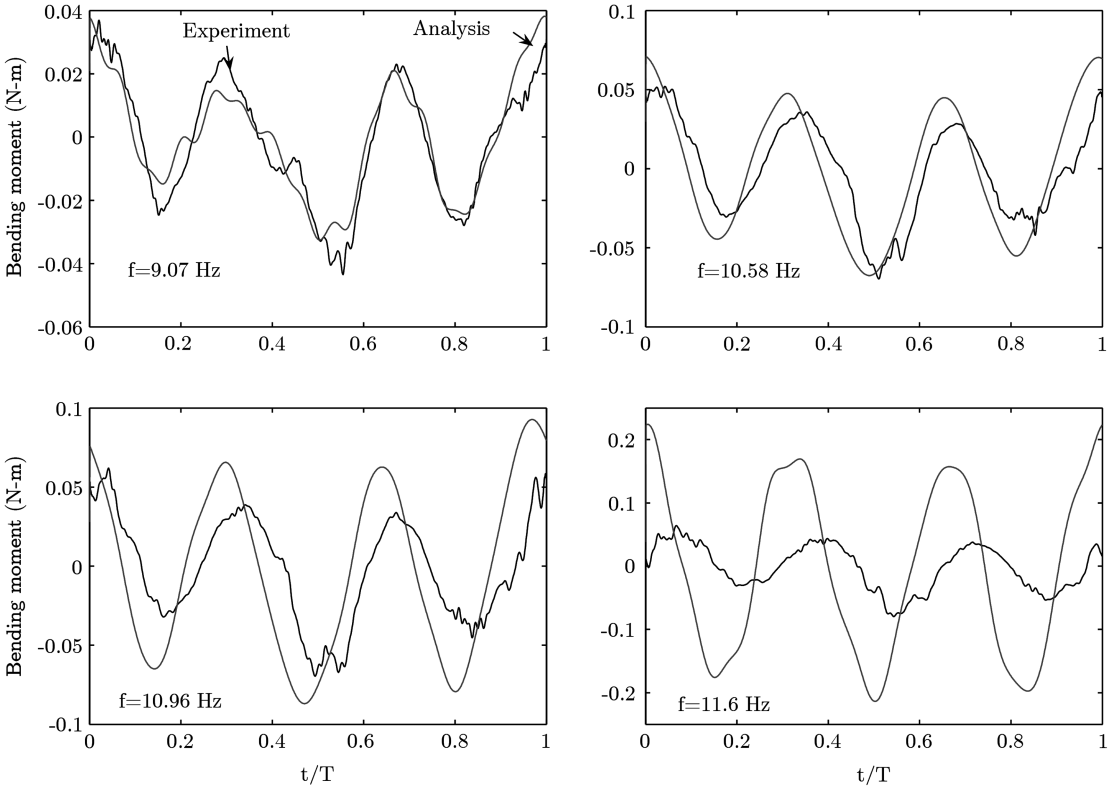

Fig. 40 Bending moment variation compared with experimental data at various flapping frequencies.

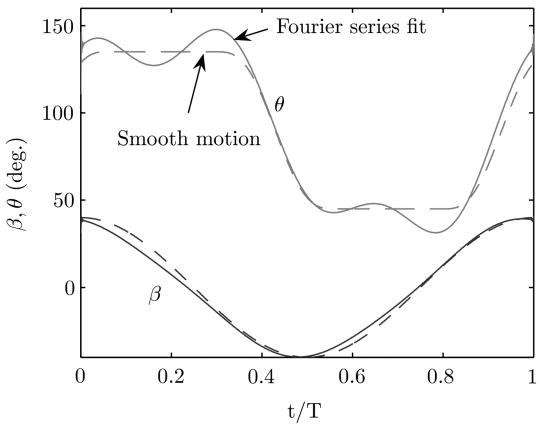

Fig. 41 Smooth motion vs Fourier series fit.

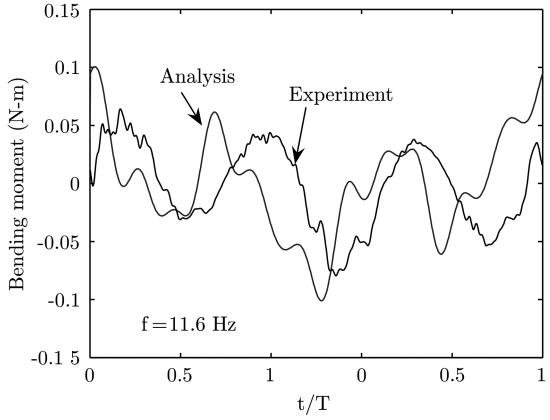

Fig. 42 Comparison of analysis and experiment at 11.6 Hz with smooth motion.

computed under inertial loading alone. These deformations were then used in the aerodynamic analysis to determine the thrust generated by the wing.

High-Frequency Tests (Wing III)

Wing III produced a maximum thrust of approximately 0.06 N at a frequency of 11 Hz and a pitch angle of 45 deg. This was the highest thrust generated among all the wings tested on the biomimetic flapping–pitching mechanism. However, this thrust dropped suddenly as the frequency was increased to 11.6 Hz. For this reason, this wing was used to ascertain the predictive capability of the present analysis. Figures 43 and 44 show the comparisons between experiment and analysis for the high-frequency tests conducted on wing III. These figures show analytical results for both a rigid wing and an elastic wing. It must be noted that, in the experiments, the wing was always elastic. Also, the results were computed using both types of input motions for the analysis, that is, the approximated motion and the smooth motion.

It is evident from Fig. 43 that the approximated motion caused a significant reduction in the thrust generated by the mechanism as compared to the smooth motion. Also, the thrust predicted by the analysis using an approximated motion agreed closely with the measured thrust, except at the highest frequency of 11.6 Hz. Using the approximated motion, an elastic wing analysis showed close agreement with the experimental results, although there was a slight overprediction of thrust at 10.96 Hz (Fig. 44). However, the most important result is that, for both the elastic cases, the analysis showed a drop in thrust at a frequency of 11.6 Hz. For these cases, the inflow did not converge because of the effect of the shed wake.

Figures 45 and 46 show the contribution of various components of the analysis to the predicted thrust at the two highest frequencies. Figure 45 shows that wing elastic deformations significantly increased the circulatory lift. This was a combined effect of an increase in the wing velocity in phase with the flapping velocity, and, changes in wing camber. However, the large accelerations introduced by wing elasticity significantly reduced the non-circulatory contribution to the thrust. The reason for a drop in wing thrust at 11.6 Hz can be understood from Fig. 46. For an elastic wing,

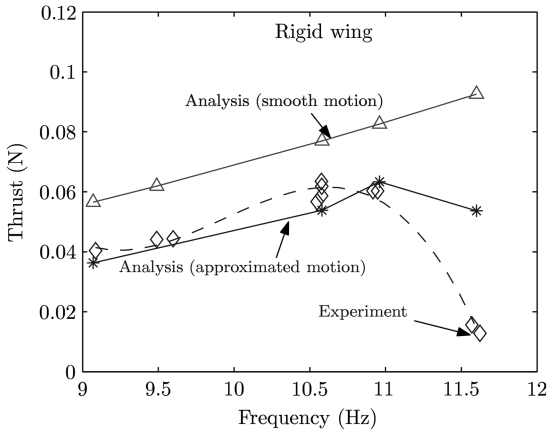

Fig. 43 Rigid wing: predicted and measured thrust.

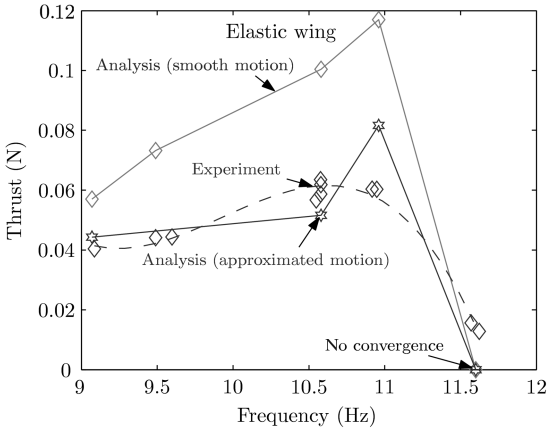

Fig. 44 Elastic wing: predicted and measured thrust.

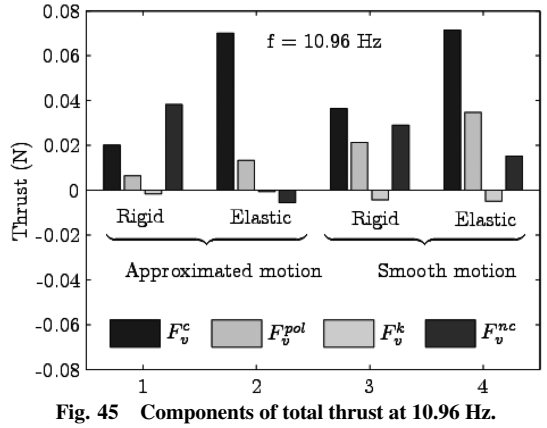

Fig. 45 Components of total thrust at 10.96 Hz.

this figure shows the components after the first iteration only, since the inflow did not converge. The noncirculatory forces introduced by wing elasticity at this frequency caused a significant reduction in the total thrust. This led to a reduced inflow, which brought the shed wake closer to the wing plane. The vorticity in the shed wake was quite strong because of the significant circulatory forces. The close proximity of this vorticity to the wing plane was the primary cause for nonconvergence of the inflow.

Low-Frequency Tests

Figure 47 shows a comparison between the analysis and experiment, for low-frequency tests carried out on wing III at a pitch angle of 45 deg. For reference, the high-frequency results are also

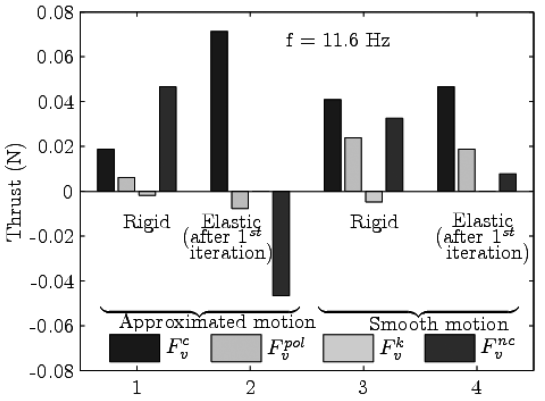

Fig. 46 Components of total thrust at 11.6 Hz.

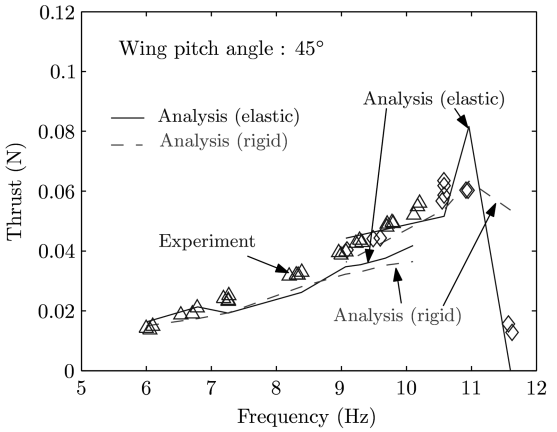

Fig. 47 Comparison of experiment and analysis for wing III at 45-deg pitch angle.

shown in this figure. For the low-frequency tests, only the pitch motion was measured, hence, flapping position data were unavailable. For these cases, the flap motion was assumed to be similar to the high-frequency tests. Because the approximated motion showed satisfactory prediction of the low-frequency bending moment, all the results in this section were obtained using the approximated motion. Figure 47 shows good agreement between experiment and analysis at low frequencies, but there is some underprediction of thrust at the higher frequencies. For these frequencies, an elastic analysis improved prediction. The difference between the low-frequency and high-frequency predictions near 10 Hz is because the flap motion was not measured in the low-frequency tests. Figure 48 shows a comparison between experiment and analysis for wing III at a pitch angle of 30 deg. For this case, good agreement is seen with experimental data, for both rigid and elastic analyses. The elastic analysis overpredicts the thrust at certain frequencies. This may be caused by some error in the computed deformations because of an assumed flap motion, because the flap motion was not measured in this case.

Figure 49 shows a comparison of experiment and analysis for the thrust produced by wing II at 30 and 45-deg pitch angles. This wing was characterized by its pitching axis, which was located at the 50% chord location as compared to the 20% chord location for wing III. For both pitch angles, the rigid analysis slightly overpredicted the thrust. The elastic analysis also overpredicted the thrust at 30-deg pitch angle, but prediction improved at 45-deg pitch angle. However, an interesting observation from these results is that, unlike wing III, an increase in pitch angle did not result in an increase in thrust. This effect was captured by the analysis. To examine this closely, Fig. 50 shows the components of the total thrust, as predicted by the analysis, at the two pitch angles. For the rigid case, the circulatory force increased with the wing pitch angle, as expected. However, the noncirculatory force reduced with an increase in pitch angle, keeping

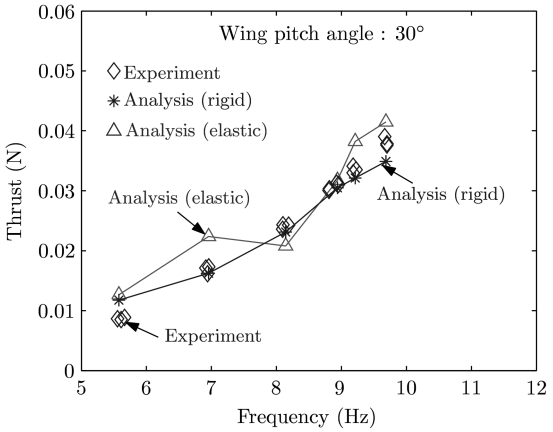

Fig. 48 Comparison of experiment and analysis for wing III at 30-deg pitch angle.

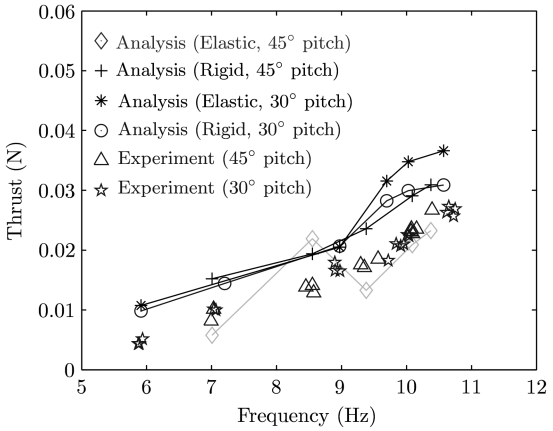

Fig. 49 Comparison of experiment and analysis for wing II at 30 and 45-deg pitch angles.

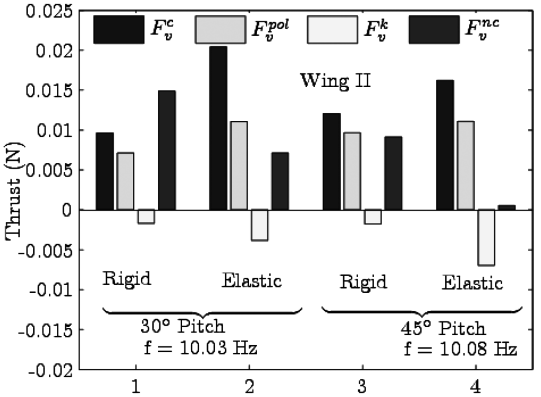

Fig. 50 Components of total thrust for wing II at 30 and 45-deg pitch angles.

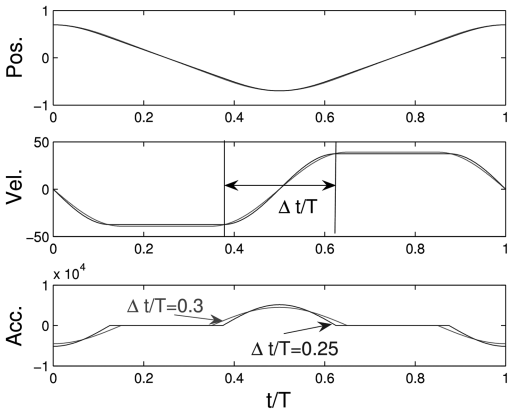

Fig. 51 Input flap motion showing duration of acceleration.

the total thrust nearly constant. For the elastic case, both the circulatory and noncirculatory forces showed a reduction with increasing pitch angle, leading to a lower overall thrust at the higher pitch angle. The Kussner force depends on two main factors: 1) the strength of shed vorticity in the wake and 2) on the inflow velocity which determines the spacing of the shed wake below the wing. The strength of shed vorticity was dependent on the total circulatory lift, while the inflow depended on the total thrust, which in turn, depended on all the components of thrust. This is why an iterative scheme was used for convergence. For the 45-deg elastic case, in Fig. 27, the overall circulatory force increased as compared to the rigid analysis, which increased the strength of the shed vorticity in the wake. In addition, the noncirculatory component reduced to nearly zero. The combined effect was a stronger wake, closer to the wing, which led to a more negative Kussner lift component.

Aerodynamic Center of Pressure

In the experiments conducted on the flapping wings, it was assumed that the net aerodynamic force acts at the point defined by the second moment of area of the wing. This point was at a distance of 10.34 cm from the flapping axis. From the analytical predictions, the center of pressure of the airloads was found to be at distances of 9.52 and 11.03 cm from the flapping axis, for the rigid and elastic analyses, respectively. For the elastic case, this represents an error of 6.9 mm in the estimation of the location of the center of pressure. At maximum thrust, this error would lead to a 6.2% reduction in thrust.

High-Frequency Bending Moment

To investigate the error in the bending moment prediction at a high frequency, several tests were conducted with the wing in pure flapping motion. Because of the absence of active pitching, these tests could be conducted at higher frequencies (up to 17 Hz). A similar bending moment discrepancy was noticed in these tests. However, this discrepancy was present in a narrow band of frequency (∼10.5–13.5 Hz). At higher frequencies, the predictions improved considerably. Figure 51 shows the smooth motion input used in the analysis. A systematic evaluation of the problem showed that the wing response was greatly influenced by small changes in the duration of wing acceleration (Fig. 51). Small changes in this duration do not show any significant change in the wing position, as shown in Fig. 51. Based on this, the input motion for the combined flapping–pitching wing was modified slightly by increasing $\Delta t/T$ to 0.3. Figure 52 shows the improved bending moment prediction at high frequency. Figure 53 shows the thrust computed using this improved analysis. The overprediction of thrust, caused by the error in wing response, was considerably improved at a frequency of 10.96 Hz.

The wing deformations were not measured experimentally. However, the analysis showed tip deflections greater than 5 cm at the higher frequencies. Although a nonlinear structural model would be required in such cases, the linear analysis used in this study provided good correlation with experimental data.

Coupled Analysis

To investigate the effect of airloads on wing deformation, a loose coupling procedure was implemented. In this analysis, the wing deformations were first computed without the aerodynamic loads. Using these deformations, the airloads were computed. These airloads were then applied to the wing and its deformations were recomputed until the wing response converged. It must be noted that the wing finite element grid points were used in the aerodynamic analysis as well. This simplified the coupling procedure to a great extent. Also, the effect of aerodynamic pitching moment on wing

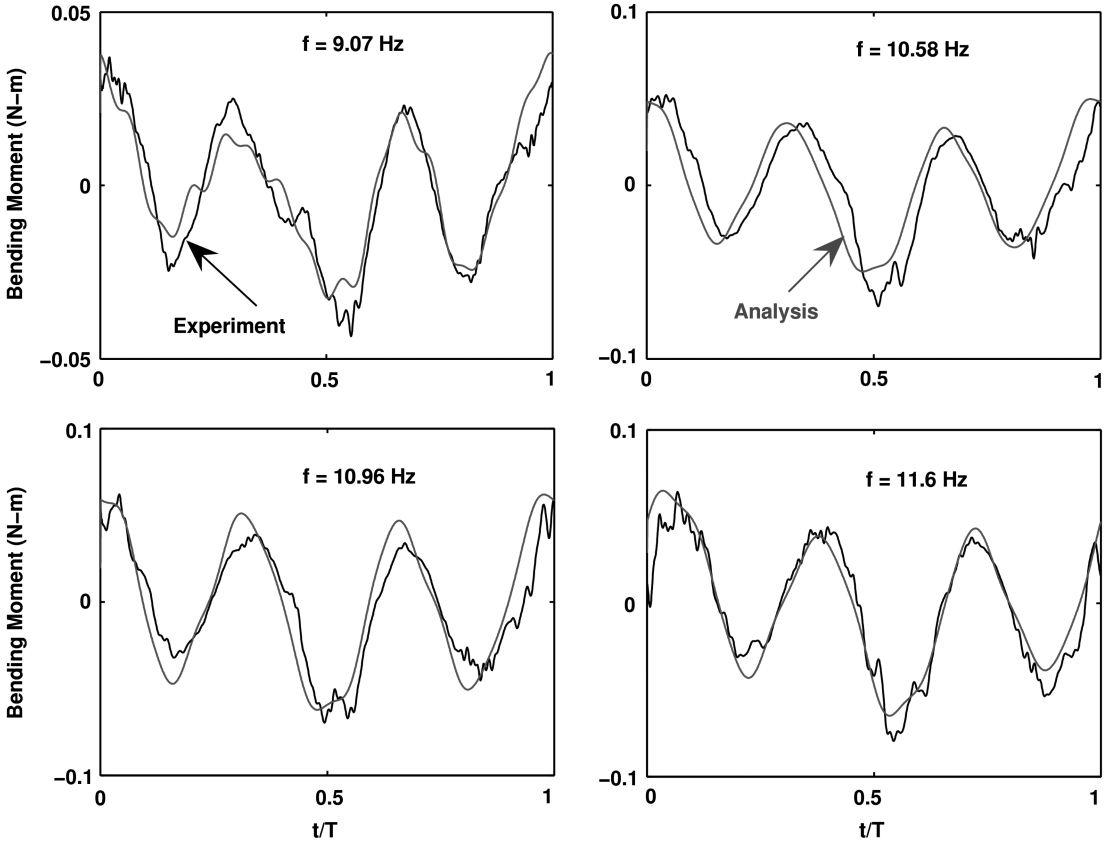

Fig. 52 Improved bending moment prediction.

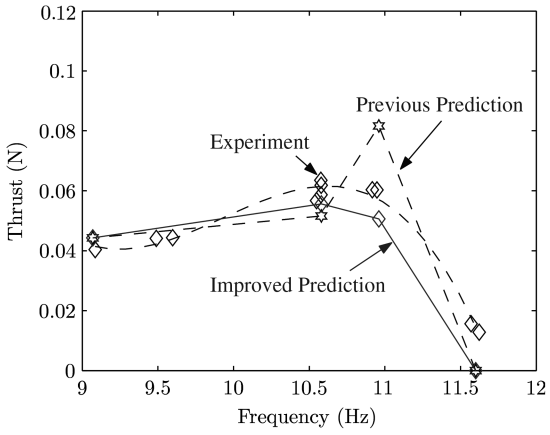

Fig. 53 Improved thrust prediction.

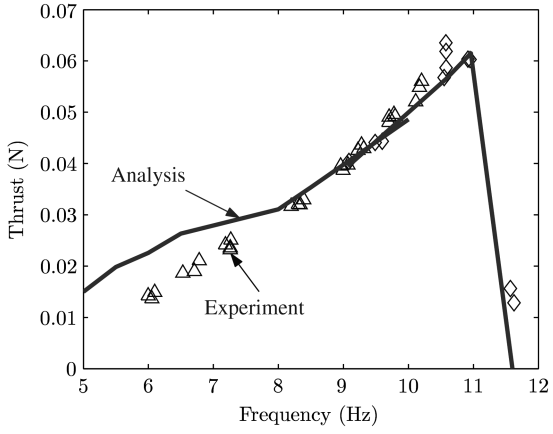

Fig. 54 Thrust prediction with coupled analysis for wing III.

twist was neglected in this analysis. Figure 54 shows the thrust computed using the coupled analysis at both low and high frequencies. Good agreement was seen with experimental data, although there was a slight overprediction at low frequencies. The most likely reason for this overprediction is that the smooth flap motion used in the analysis does not mimic the actual flap motion very well because this flap motion was not measured. Figure 55 shows a comparison of the bending moment computed using the uncoupled and coupled analyses. Identical smooth motions were input to the analysis in each case. These results show that, although the overall bending moment variation was governed by the inertial forces, the aerodynamic loads did affect this variation. Thus, for the wings used in this study, the aerodynamic forces cannot be neglected in the wing response computation, although they do not have a significant effect on the average thrust.

Summary and Conclusions

The thrust generated by a number of wings, mounted on a flapping–pitching mechanism, was measured for a number of wing and stroke parameters. A wing pitching about its 20% chord location (wing III) produced more thrust, because of higher rotational circulation during the pronation and supination phases, as compared to a wing which pitched about its midchord (wing II). When the pitch angle of the wings was increased from 30 to 45 deg, the thrust produced by wing III increased, but the thrust for wing II remained the same. In the low-frequency tests, wing III generated the maximum thrust at a pitch angle of 45 deg.

To increase the measured thrust, wing III was tested at higher frequencies. The mass of the wing was found to have a large impact on the maximum frequency attainable with the mechanism. However, the measured thrust showed a sudden drop when the flapping frequency was increased to 11.6 Hz. A number of light

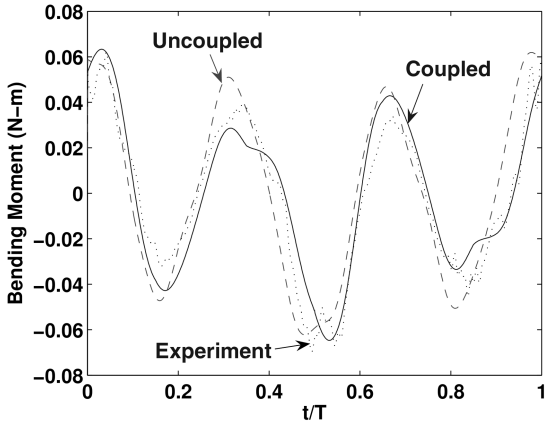

Fig. 55 Comparison of bending moments calculated using coupled and uncoupled analyses.

composite wings were also manufactured and tested at high frequencies. However, all these wings showed a drop in thrust at high frequencies. By measuring the stroke position of the wings, the total aerodynamic and inertial power was computed at the base of the wing using the measured loads. The effect of wing mass on power required was also evident from the power curves.

Preliminary tests for a pure flapping motion with passive pitching of the shaft because of the inertial and aerodynamic forces acting on the wing showed significant thrust generation by one of the wings tested. In this case, the wing was held at a 90-deg angle and flapped in a horizontal plane. Because of the pitch flexibility of the shaft, the inertial and aerodynamic forces caused the shaft to pitch in a passive manner. To further explore the lift generation capability of a passive-pitch flapping wing mechanism, the biomimetic flapping–pitching mechanism was modified to include a torsion spring on the flapping shaft. The torsional stiffness of the spring could be easily adjusted from a stiff condition to a soft one. When the spring was kept in the soft position the pitch variation was larger than the pitch variation for a stiff spring. Also, the larger pitch variation for the soft spring helped generate greater thrust at a slightly smaller power consumption than the stiff spring. Such a passive-pitch mechanism merits further study because its mechanical simplicity makes it easier to implement on an actual MAV.

An aeroelastic analysis was also developed for flapping wings and compared with the experimental measurements presented in this paper. A validation of the aerodynamic analysis was carried out by comparing the analytical prediction of thrust with experimental data available in literature. These experiments, conducted on wings moving at very low frequency in oil [11], are ideal for validating the aerodynamic analysis without elastic effects. The experimentally measured lift and drag coefficients had to be used in the analysis for improved force prediction. These coefficients were 3-D in nature, however, nearly identical coefficients were obtained by Wang et al. [48] using a 2-D analysis. At the beginning of each half-stroke, a force peak was observed in the analysis. This peak was primarily caused by noncirculatory forces. This force peak explained, at least in part, the force peak observed in the experiment. However, in [11] this peak was attributed to wake capture alone, based on the improper assumption that, for a flat stroke plane noncirculatory forces could not affect the vertical force.

Data from the high-frequency biomimetic flapping mechanism were used to validate the structural analysis for the combined flapping and pitching motion of lightweight, aluminum-Mylar wings. An accurate measurement of the flapping and pitching accelerations was essential for good agreement between experiment and analysis. These accelerations were provided as inputs to the analysis. However, only the flapping and pitch position data were available from the experiments. To overcome this problem, a Fourier series was fit to the measured motion, and, from this fit, the velocity and acceleration were approximated. Because the measured and approximate motions had significant variations from a smooth flapping motion, the analysis was also carried out with a smooth motion. At high frequencies, the predicted bending moment had significant errors. This discrepancy was resolved and a coupled analysis was carried out with loose coupling between the structural and aerodynamic parts. Some important conclusions from this study are as follows:

1) The rigid wing analysis was unable to predict the drop in thrust at high frequency. However, the elastic analysis predicted this drop, for both approximate and smooth motion inputs.

2) Wing elasticity led to a significant increase in the circulatory thrust because of the higher effective wing velocity. However, this increase was offset by a reduction in the thrust produced by noncirculatory forces. In fact, it is this reduction that caused the drop in thrust at high frequency.

3) At a high frequency, the large negative noncirculatory thrust caused by wing elasticity led to convergence problems for the inflow. This was because a low thrust produced a low inflow velocity, which brought the strong shed wake in close proximity to the wing.

4) The bending moment error at a high frequency was found to be caused by the duration of wing acceleration in a flapping cycle. With an improvement in bending moment prediction, the thrust prediction was also improved.

5) A coupled analysis did not have significant effect on the average thrust. However, the bending moment predictions were significantly altered. This shows that the aerodynamic loads cannot be neglected in computing the wing response.

In the present study we showed that wing flexibility plays a key role in the thrust generating capability of MAV scale flapping wings. Further experimentation and analytical studies are required to determine the optimum configuration for such flapping wings.

Acknowledgments

This research work was supported by the Army Research Office through the Micro Air Vehicle, Multidiciplinary University Research Initiative (MAV MURI) Program (Grant No. ARMY-W911NF0410176) with Gary Anderson and Thomas Doligalski as the Technical Monitors. The authors also wish to acknowledge the contribution of Matthew Tarascio (now with Sikorsky Aircraft) in building the flapping wing mechanism.

References

[1] McMichael, J. M., and Francis, M. S., *Micro Air Vehicles—Toward a New Dimension in Flight*, Defence Advanced Research Projects Agency TTO Document, 1996.

[2] Grasmeyer, J. M., and Keennon, M. T., "Development of the Black Widow Micro Air Vehicle," *39th AIAA Aerospace Sciences Meeting and Exhibit*, AIAA, Reston, VA, 8–11 Jan. 2001.

[3] Bohorquez, F., Samuel, P., Sirohi, J., Pines, D., Rudd, L., and Perel, R., "Design, Analysis and Hover Performance of a Rotary Wing Micro Air Vehicle," *Journal of the American Helicopter Society*, Vol. 48, No. 2, April 2003, pp. 80–90.

[4] Keennon, M. T., and Grasmeyer, J. M., "Development of the Black Widow and Microbat MAVs and a Vision of the Future of MAV Design," *AIAA/ICAS International Air and Space Symposium and Exposition: The Next 100 Years*, AIAA, Reston, VA, 14–17 July 2003.

[5] Ellington, C. P., "The Aerodynamics of Hovering Insect Flight," *Philosophical Transactions of the Royal Society of London. Series B: Biological Sciences*, Vol. 305, No. 1122, Feb. 1984, pp. 1–181. doi:10.1098/rstb.1984.0049

[6] Willmott, A. P., and Ellington, C. P., "The Mechanics of Flight in the Hawkmoth Manduca Sexta I. Kinematics of Hovering and Forward Flight," *Journal of Experimental Biology*, Vol. 200, No. 21, 1997, pp. 2705–2722.

[7] Altshuler, D. L., and Dudley, R., "Kinematics of Hovering Hummingbird Flight Along Simulated and Natural Elevational Gradients," *Journal of Experimental Biology*, Vol. 206, Aug. 2003, pp. 3139–3147. doi:10.1242/jeb.00540

[8] Wang, H., Zeng, L., Liu, H., and Yin, C., "Measuring Wing Kinematics, Flight Trajectory and Body Attitude During Forward Flight and Turning Maneuvers in Dragonflies," *Journal of Experimental Biology*, Vol. 206, No. 4, Feb. 2003, pp. 745–757. doi:10.1242/jeb.00183

[9] van den Berg, C., and Ellington, C. P., "The Vortex Wake of a 'Hovering' Model Hawkmoth," *Philosophical Transactions of the Royal Society of London. Series B: Biological Sciences*, Vol. 352, No. 1351, March 1997, pp. 317–328. doi:10.1098/rstb.1997.0023

[10] van den Berg, C., and Ellington, C. P., "The Three-Dimensional Leading-Edge Vortex of a 'Hovering' Model Hawkmoth," *Philosophical Transactions of the Royal Society of London. Series B: Biological Sciences*, Vol. 352, No. 1351, March 1997, pp. 329–340. doi:10.1098/rstb.1997.0024

[11] Dickinson, M. H., Lehmann, F., and Sane, S. P., "Wing Rotation and the Aerodynamic Basis of Insect Flight," *Science*, Vol. 284, June 1999, pp. 1954–1960. doi:10.1126/science.284.5422.1954

[12] Weis-Fogh, T., "Quick Estimates of Flight Fitness in Hovering Animals, Including Novel Mechanisms for Lift Production," *Journal of Experimental Biology*, Vol. 59, No. 1, 1973, pp. 169–230.

[13] Liu, H., Ellington, C. P., Kawachi, K., van den Berg, C., and Willmott, A. P., "A Computational Fluid Dynamic Study of Hawkmoth Hovering," *Journal of Experimental Biology*, Vol. 201, No. 4, 1998, pp. 461–477.

[14] Sane, S. P., "The Aerodynamics of Insect Flight," *Journal of Experimental Biology*, Vol. 206, No. 23, Dec. 2003, pp. 4191–4208. doi:10.1242/jeb.00663

[15] Ellington, C. P., and Usherwood, J. R., "Lift and Drag Characteristics of Rotary and Flapping Wings," *Fixed and Flapping Wing Aerodynamics for Micro Air Vehicle Applications*, edited by T. J. Mueller, Vol. 195, AIAA Progress in Aeronautics and Astronautics, AIAA, Reston, VA, 2001, pp. 231–248, Chap. 12.

[16] Birch, J. M., Dickson, W. B., and Dickinson, M. H., "Force Production and Flow Structure of the Leading Edge Vortex on Flapping Wings at High and Low Reynolds Numbers," *Journal of Experimental Biology*, Vol. 207, Feb. 2004, pp. 1063–1072. doi:10.1242/jeb.00848

[17] Ramasamy, M., Leishman, J. G., and Singh, B., "Wake Structure Diagnostics of a Flapping Wing MAV," *International Powered Lift Conference*, SAE International, Warrendale, PA, Oct. 2005.

[18] Lan, C. E., "The Unsteady Quasi-Vortex-Lattice Method with Applications to Animal Propulsion," *Journal of Fluid Mechanics*, Vol. 93, No. 4, 1979, pp. 747–765. doi:10.1017/S0022112079002019

[19] Wang, Z. J., "Vortex Shedding and Frequency Selection in Flapping Flight," *Journal of Fluid Mechanics*, Vol. 410, May 2000, pp. 323–341. doi:10.1017/S0022112099008071

[20] Birch, J. M., and Dickinson, M. H., "The Influence of Wing Wake Interactions on the Production of Aerodynamic Forces in Flapping Flight," *Journal of Experimental Biology*, Vol. 206, No. 13, July 2003, pp. 2257–2272. doi:10.1242/jeb.00381

[21] Żbikowski, R., "On Aerodynamic Modelling of an Insect-Like Flapping Wing in Hover for Micro Air Vehicles," *Philosophical Transactions of the Royal Society London, Series A*, Vol. 360, Jan. 2002, pp. 273–290. doi:10.1098/rsta.2001.0930

[22] DeLaurier, J. D., "An Aerodynamic Model for Flapping Wing Flight," *Aeronautical Journal*, Vol. 97, April 1993, pp. 125–130.

[23] Larijani, R. F., and DeLaurier, J. D., "A Nonlinear Aeroelastic Model for the Study of Flapping Wing Flight," *Fixed and Flapping Wing Aerodynamics for Micro Air Vehicle Applications*, edited by T. J. Mueller Vol. 195, AIAA Progress in Aeronautics and Astronautics, AIAA, Reston, VA, 2001, pp. 399–428, Chap. 18.

[24] Fritz, T. E., and Long, L. N., "Object-Oriented Unsteady Vortex Lattice Method for Flapping Flight," *Journal of Aircraft*, Vol. 41, No. 6, Nov.–Dec. 2004, pp. 1275–1290.

[25] Eldredge, J. D., "Efficient Tools for the Simulation of Flapping Wing Flows," *43rd AIAA Aerospace Sciences Meeting and Exhibit*, AIAA, Reston, VA, 10–13 Jan. 2005.

[26] Sun, M., and Tang, J., "Unsteady Aerodynamic Force Generation by a Model Fruit Fly Wing in Flapping Motion," *Journal of Experimental Biology*, Vol. 205, No. 1, Jan. 2002, pp. 55–70.

[27] Sun, M., and Tang, J., "Lift and Power Requirements of Hovering Flight in Drosophila Virilis," *Journal of Experimental Biology*, Vol. 205, No. 16, Aug. 2002, pp. 2413–2427.

[28] Ramamurti, R., and Sandberg, W. C., "A Three-Dimensional Computational Study of the Aerodynamic Mechanisms of Insect Flight," *Journal of Experimental Biology*, Vol. 205, No. 10, May 2002, pp. 1507–1518.

[29] Sun, M., and Wu, J. H., "Aerodynamic Force Generation and Power Requirements in Forward Flight in a Fruit Fly with Modeled Wing Motion," *Journal of Experimental Biology*, Vol. 206, No. 17, Sept. 2003, pp. 3065–3083. doi:10.1242/jeb.00517

[30] Wu, J. H., and Sun, M., "Unsteady Aerodynamic Forces of a Flapping Wing," *Journal of Experimental Biology*, Vol. 207, No. 23, March 2004, pp. 1137–1150. doi:10.1242/jeb.00868

[31] Wang, Z. J., "The Role of Drag in Insect Hovering," *Journal of Experimental Biology*, Vol. 207, No. 23, Nov. 2004, pp. 4147–4155. doi:10.1242/jeb.01239

[32] Ramamurti, R., Sandberg, W. C., Lohner, R., Walker, J. A., and Westneat, M. W., "Fluid Dynamics of Flapping Aquatic Flight in the Bird Wrasse: Three-Dimensional Unsteady Computations with Fin Deformation," *Journal of Experimental Biology*, Vol. 205, No. 19, Oct. 2002, pp. 2997–3008.

[33] Bozkurttas, M., Dong, H., Mittal, R., Madden, P., and Lauder, G. V., "Hydrodynamic Performance of Deformable Fish Fins and Flapping Foils," *44th AIAA Aerospace Sciences Meeting and Exhibit*, AIAA, Reston, VA, 9–12 Jan. 2006.

[34] Wootton, R. J., "The Mechanical Design of Insect Wings," *Scientific American*, Vol. 263, Nov. 1990, pp. 114–120.

[35] Wootton, R. J., Herbert, R. C., Young, P. G., and Evans, K. E., "Approaches to the Structural Modeling of Insect Wings," *Philosophical Transactions of the Royal Society of London. Series B: Biological Sciences*, Vol. 358, Aug. 2003, pp. 1577–1587. doi:10.1098/rstb.2003.1351

[36] Tarascio, M. J., and Chopra, I., "Design and Development of a Thrust Augmented Entomopter: An Advanced Flapping Wing Micro Hovering Air Vehicle," *Proceedings of the 59th Annual Forum of the American Helicopter Society*, AHS International, Alexandria, VA, May 2003.

[37] Singh, B., Ramasamy, M., Chopra, I., and Leishman, J. G., "Insect Based Flapping Wings for Micro Hovering Air Vehicles: Experimental Investigations," *American Helicopter Society International Specialists Meeting on Unmanned Rotorcraft*, AHS International, Alexandria, VA, Jan. 2005.

[38] Singh, B., and Chopra, I., "Wing Design and Optimization for a Flapping Wing Micro Air Vehicle," *60th Annual Forum of the American Helicopter Society*, AHS International, Alexandria, VA, June 2004.

[39] Banerjee, A. K., and Kane, T. R., "Dynamics of a Plate in Large Overall Motion," *Journal of Applied Mechanics*, Vol. 56, No. 14, Dec. 1989, pp. 887–892.

[40] Banerjee, A. K., and Dickens, J. M., "Dynamics of an Arbitrary Flexible Body in Large Rotation and Translation," *Journal of Guidance, Control, and Dynamics*, Vol. 13, No. 2, March 1990, pp. 221–227.

[41] Jinyang, L., and Jiazhen, H., "Geometric Nonlinear Formulation and Discretization Method for a Rectangular Plate Undergoing Large Overall Motions," *Mechanics Research Communications*, Vol. 32, No. 5, Sept. 2005, pp. 561–571. doi:10.1016/j.mechrescom.2004.10.007

[42] Reddy, J. N., *Mechanics of Laminated Composite Plates*, CRC Press, Boca Raton, FL, 1997.

[43] Polhamus, E. C., "A Concept of the Vortex Lift of Sharp Edge Delta Wings Based on a Leading-Edge Suction Analogy," NASA TN D-3767, 1966.

[44] Katz, J., and Plotkin, A., *Low-Speed Aerodynamics*, Cambridge Univ. Press, Cambridge, England, U.K., 2001.

[45] Polhamus, E. C., "Predictions of Vortex-Lift Characteristics by a Leading-Edge Suction Analogy," *Journal of Aircraft*, Vol. 8, No. 4, April 1971, pp. 193–199.

[46] Purvis, J. W., "Analytical Prediction of Vortex Lift," *Journal of Aircraft*, Vol. 18, No. 4, April 1981, pp. 225–230.

[47] Leishman, J. G., *Helicopter Aerodynamics*, Cambridge Univ. Press, Cambridge, England, U.K., 2000.

[48] Wang, Z. J., Birch, J. M., and Dickinson, M. H., "Unsteady Forces and Flows in Low Reynolds Number Hovering Flight: Two-Dimensional Computations vs Robotic Wing Experiments," *Journal of Experimental Biology*, Vol. 207, No. 3, Feb. 2004, pp. 449–460. doi:10.1242/jeb.00739

[49] Daniel, T. L., and Combes, S. A., "Flexible Wings and Fins: Bending by Inertial or Fluid Dynamic Forces?," *Integrative and Comparative Biology*, Vol. 42, No. 5, 2002, pp. 1044–1049. doi:10.1093/icb/42.5.1044

C. Cesnik
Associate Editor